

## APPLIED SCIENCES AND ENGINEERING

# Waterproof, electronics-enabled, epidermal microfluidic devices for sweat collection, biomarker analysis, and thermography in aquatic settings

Jonathan T. Reeder<sup>1,2</sup>, Jungil Choi<sup>1,2</sup>, Yeguang Xue<sup>3,4</sup>, Philipp Gutruf<sup>1,2</sup>, Justin Hanson<sup>5</sup>, Mark Liu<sup>6</sup>, Tyler Ray<sup>1,2</sup>, Amay J. Bandodkar<sup>1,2</sup>, Raudel Avila<sup>3,4</sup>, Wei Xia<sup>3,7</sup>, Siddharth Krishnan<sup>8</sup>, Shuai Xu<sup>2,9</sup>, Kelly Barnes<sup>10</sup>, Matthew Pahnke<sup>10</sup>, Roozbeh Ghaffari<sup>2,6,11</sup>, Yonggang Huang<sup>1,3,4</sup>, John A. Rogers<sup>1,2,4,6,12,13\*</sup>

Copyright © 2019  
The Authors, some  
rights reserved;  
exclusive licensee  
American Association  
for the Advancement  
of Science. No claim to  
original U.S. Government  
Works. Distributed  
under a Creative  
Commons Attribution  
NonCommercial  
License 4.0 (CC BY-NC).

Noninvasive, in situ biochemical monitoring of physiological status, via the use of sweat, could enable new forms of health care diagnostics and personalized hydration strategies. Recent advances in sweat collection and sensing technologies offer powerful capabilities, but they are not effective for use in extreme situations such as aquatic or arid environments, because of unique challenges in eliminating interference/contamination from surrounding water, maintaining robust adhesion in the presence of viscous drag forces and/or vigorous motion, and preventing evaporation of collected sweat. This paper introduces materials and designs for waterproof, epidermal, microfluidic and electronic systems that adhere to the skin to enable capture, storage, and analysis of sweat, even while fully underwater. Field trials demonstrate the ability of these devices to collect quantitative in situ measurements of local sweat chloride concentration, local sweat loss (and sweat rate), and skin temperature during vigorous physical activity in controlled, indoor conditions and in open-ocean swimming.

## INTRODUCTION

Recent advances in materials science and mechanics design serve as the foundations for emerging classes of thin, soft devices that can interface with the surface of the skin for multifunctional sensing of body processes. For biochemical evaluations, sweat represents an interesting but relatively underexplored biofluid that contains various biomarkers of core relevance to assessments of physiological health. Knowledge of athletes' sweat composition, rate of sweat loss, and total sweat fluid and electrolyte loss is important in maintaining proper hydration levels and electrolyte balance in athletic competition/training and in other physically demanding activities. These same parameters can be valuable in various areas of clinical medicine (1, 2). Wearable electrochemical sensors enable real-time evaluation of sweat biomarker concentrations (3–9), where hydrogel-, paper-, or textile-based materials passively route sweat to sensing electrodes that interface to recording electronics, power supply systems, and radio communication hardware. These approaches do not, however, in-

corporate microfluidic technologies, and they are therefore unable to support many important operations in fluidic manipulation for precise capture, storage, volumetric measurement, and chemical analysis. Most embodiments also do not effectively isolate sweat from the skin and the surrounding environment (10, 11), thereby limiting the ability to seal the sweat from contaminants and to allow for subsequent extraction and sampling. Sophisticated lab-on-a-chip-type microfluidic platforms that are thin, mechanically soft, and skin-compatible are, therefore, of particular recent interest because of their capacity to collect, route, and chemically analyze precise, micro-liter volumetric samples of sweat released from well-defined regions of the skin (12–15).

The specific focus of the current work is on athletics and fitness, where personalized hydration strategies are important because of wide variations of sweat rate and composition across individuals, settings, and circumstances (16). Dryland athletes in hot environments often do not adequately replenish fluid loss due to perspiration, leading to hyperosmotic hypovolemia (17). While sweating rate in swimmers is typically lower than that for dryland athletes, it can range from 0.33 to 1.6 liter/hour (18–21), depending on the water temperature (22) and exercise intensity (18). While smaller amounts of unreplaced sweat losses may not alter short-duration swimming performance, the risk for subsequent exercise dehydration in events such as ultra-endurance triathlons may make it more challenging to maintain euhydration. Proper hydration is important, as underdrinking can lead to hypohydration and overdrinking can lead to hyponatremia (low serum sodium concentration) (23) and other complications. Ultra-endurance athletes are particularly susceptible to hyponatremia (24), where the incidence of symptomatic hyponatremia has been up to ~1% (23), while asymptomatic cases have been reported as high as 27% for ultramarathoners (25), up to 25% for IRONMAN triathletes (26), and up to 17% for swimmers after a 26.4-km race (27). As a result, the American College of Sports Medicine recommends measurements of body weight to monitor hydration status changes during

<sup>1</sup>Department of Materials Science and Engineering, McCormick School of Engineering, Northwestern University, Evanston, IL 60208, USA. <sup>2</sup>Center for Bio-Integrated Electronics, Northwestern University, Evanston, IL 60208, USA. <sup>3</sup>Department of Civil and Environmental Engineering, McCormick School of Engineering, Northwestern University, Evanston, IL 60208, USA. <sup>4</sup>Department of Mechanical Engineering, McCormick School of Engineering, Northwestern University, Evanston, IL 60208, USA. <sup>5</sup>Department of Biological Sciences, Feinberg School of Medicine, Northwestern University, Chicago, IL 60611 USA. <sup>6</sup>Department of Biomedical Engineering, McCormick School of Engineering, Northwestern University, Evanston, IL 60208, USA. <sup>7</sup>State Key Laboratory for Strength and Vibration of Mechanical Structures, Xi'an Jiaotong University, Xi'an, Shaanxi 710049, China. <sup>8</sup>Department of Materials Science and Engineering and Frederick Seitz Materials Research Laboratory, University of Illinois at Urbana-Champaign, Urbana, IL 61801, USA. <sup>9</sup>Department of Dermatology, Feinberg School of Medicine, Northwestern University, Chicago IL 60611 USA. <sup>10</sup>Gatorade Sports Science Institute, 617 W. Main St., Barrington, IL 60010, USA. <sup>11</sup>Epicore Biosystems Inc., Cambridge, MA 02139, USA. <sup>12</sup>Departments of Chemistry, and Electrical Engineering and Computer Science, McCormick School of Engineering, Northwestern University, Evanston, IL 60208, USA. <sup>13</sup>Departments of Neurological Surgery, Feinberg School of Medicine, Northwestern University, Chicago, IL 60611, USA.

\*Corresponding author. Email: jrogers@northwestern.edu

exercise (28, 29). Measurements of sweat loss from swimmers via changes in body weight are, however, intrinsically inaccurate because of inadvertent (and unmeasurable) loss of water from excretion, urination, respiration, and metabolism of substrates and gain from water ingestion and transcutaneous water absorption (30, 31). Hot environments can exacerbate the effects of improper hydration and induce heat-related illness such as heat stroke and heat exhaustions (32).

Wearable devices that provide real-time information on aquatic athletes' local sweat loss, electrolyte concentrations, and skin temperature could serve as a powerful, enabling tool for real-time management of electrolyte loss and balance and presymptomatic detection of heat-related illnesses. Waterproof absorbent pads have allowed aquatic sweat collection for postanalysis of salt levels of sweat from swimmers but only in an *ex situ* mode that requires substantial sample preparation time and expensive ancillary equipment (20). Methods for *in situ* measurements of sweat volume, sweat composition, and thermoregulation metrics for aquatic athletes do not currently exist. Skin-mounted electronic and microfluidic sensors that operate in aqueous environments could therefore address an important unmet need, with the potential to inform fluid and electrolyte replenishment strategies for improving performance, decreasing recovery time, and preventing injuries of aquatic athletes.

Here, we introduce a robust, waterproof platform with combined microfluidic and electronic functionality, designed to softly and conformally bond to the skin for real-time monitoring of key hydration metrics on performing aquatic athletes via underwater sweat collection and skin thermography. The results expand on recently introduced classes of skin-integrated microfluidic systems (33–35) that perform quantitative, multi-analyte colorimetric detection of biomarkers, in ways that are capable of collecting and analyzing sweat during aquatic exercise, even while fully submerged under water. Specifically, these technologies involve (i) elastomeric, moldable polymer materials for skin-compatible microfluidic platforms that have exceptionally low rates of penetration of water, water vapor, and water-borne chemistries from the surroundings; (ii) designs for microfluidic channels, inlets, and outlets that prevent interference or contamination from aquatic environments without impeding the in-flow of sweat; (iii) molding techniques for ultrathin, conformal devices that minimize shear stresses, associated with water impingement and motion of the skin; (iv) skin-adhesive materials and geometric designs that enable robust bonding and reliable sweat collection while underwater; and (v) approaches for integrating waterproof flexible/stretchable electronic devices that allow interrogation of the underlying tissue for additional, complementary sensing modalities (36, 37). In contexts studied here, the soft, conformal properties are particularly useful in establishing watertight seals to the skin in an unobtrusive manner. The resulting systems are quantitatively differentiated from conventional wearables where the rigid mechanical properties of the devices and associated coupling straps/bands lead to low-quality data and inability to capture and analyze sweat due to unstable, loose contacts to the skin.

## RESULTS

### Waterproof, epidermal, microfluidic, and electronics-enabled devices for sweat monitoring

The device platform consists of a waterproof combination of skin-like, or “epidermal,” microfluidic (epifluidic), and electronic systems that laminate onto the skin for capture, storage, and chemical analysis of sweat, and for digital measurement of skin temperature in aquatic and

dryland environments, including transitions between the two. The structures incorporate microchannels, a chamber that houses a colorimetric chemical reagent, electronics for wireless communication and precision temperature sensing, a set of reference color markers, and a skin-safe adhesive (Fig. 1A). A molded layer of an elastomer with properties tailored for purposes examined here, poly(styrene-isoprene-styrene) (SIS), bonds to a thin, flat sheet of SIS to define the sealed microfluidic system and to encapsulate the color markers (Fig. 1B). In designs that incorporate quantitative consideration of operational requirements, the microchannels have depths of  $\sim 220\ \mu\text{m}$  in circular serpentine geometries with 40 turns, each of which has a capacity of  $1.5\ \mu\text{l}$ , for a total volume of  $\sim 60\ \mu\text{l}$ . The colorimetric reagents consist of a food dye to facilitate visual assessment of the extent of filling of the microchannel with sweat or, alternatively, a silver chloranilate suspension that reacts with sweat to create a colorimetric response corresponding to the concentration of chloride. This reagent resides in a chamber adjacent to the inlet and reacts as sweat passes into the channel (Fig. 1C). The food dye contains red and blue water-soluble particles with different dissolution rates, thereby generating a volume-dependent color gradient as the device fills with sweat (Fig. 1D).

A flexible magnetic loop antenna, a set of near-field communication (NFC) components, and a light-emitting diode (LED) as a mode for user notification form a wireless interface to NFC-enabled devices (smartphones, tablets, etc) for transmitting digital identification codes and for reading skin temperature. Details on the circuit diagram and the fabrication processes are in Materials and Methods and fig. S1. A coating of SIS encapsulates the NFC electronics to allow robust operation for extended periods even when the device is completely submerged in water (Fig. 1E). Figure 1F illustrates wireless operation in a wet environment and shows the LED as it emits light through the microfluidic layers.

Reliable and reproducible collection of sweat during vigorous swimming and other aquatic activities, without substantial ingress of water from the surroundings, requires a combination of enabling design strategies, including the (i) microfluidic channel configuration consisting of a single outlet port, (ii) low water permeability and water absorption properties of the SIS, (iii) robust, watertight adhesion to the skin, and (iv) a small amount of “dead volume” near the outlet to accommodate pressure-induced backfilling. The trapped air in the channel leads to volumes of backfill that are typically less than  $2\ \mu\text{l}$  for swimming near the surface of the water (fig. S2), as described in detail in a subsequent section.

### Fabrication and characterization of SIS microfluidics

SIS offers a collection of physical characteristics that are highly attractive for sweat collection with epifluidic systems in aquatic environments (i.e., hydrophobicity, resistance to water transport, optical transparency, low elastic modulus, and high elasticity). The layers of SIS that define the microfluidic structures follow from casting solutions of SIS in propyl acetate against flat silicon wafers and those with lithographically defined patterns of bas-relief, both with fluorinated surfaces to prevent adhesion (Fig. 2A). For the former, the addition of titania creates a white coloration in the flat SIS layer. For the latter, the surface tension of the solution naturally creates a conformal coating on the bas-relief features as the propyl acetate evaporates (Fig. 2B). The soft, elastic yet physically robust properties of SIS allow demolding of intricate features without tearing. Mechanically punching inlet and outlet holes in the bottom and channel layers, respectively, and laminating the two together (light pressure, contact for  $\sim 30\ \text{min}$ ) define a waterproof

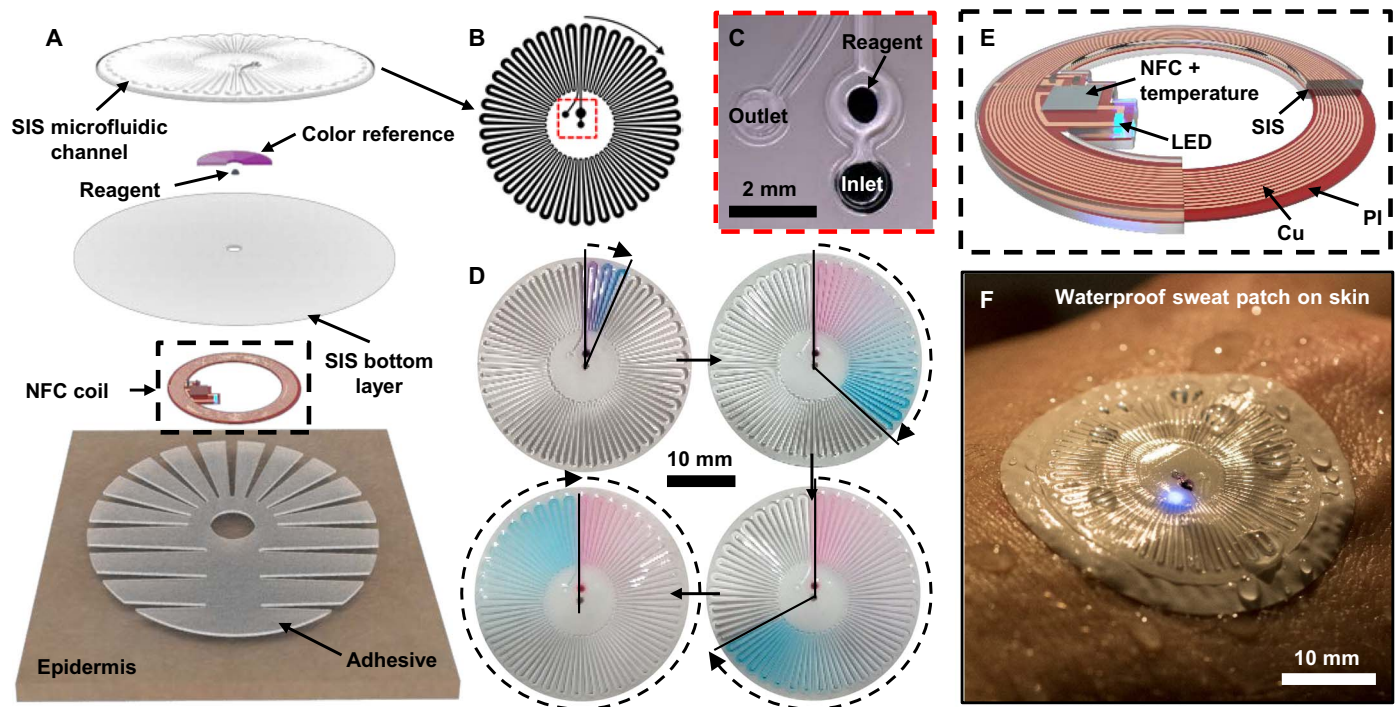


**Fig. 1. Waterproof, skin-like microfluidic/electronic device.** (A) Exploded view schematic illustration of the key layers of a representative device. (B) Microfluidic channel geometry. (C) Optical micrograph that shows the microfluidic inlet and outlet ports and the colorimetric reagent. (D) A dye composed of blue and red water-soluble particles that dissolve at different rates results in a flow-driven change in color. Measuring the number of turns of filled channels yields the total volume of collected sweat (1 turn = 1.5  $\mu\text{l}$ ). (E) Near-field communication (NFC) coil for wireless measurements of skin temperature. (F) Sweat collection in aquatic environments without contamination is enabled by the use of small outlet geometries ( $r = 0.25$  mm) and constituent polymer materials (SIS) that are hydrophobic and largely impermeable to water and water vapor. Dip coating an encapsulation of this same material enables underwater operation of the electronics, including the NFC coil, integrated circuit chip, and indicator light-emitting diode (LED). Photo credit: P. Gutruf, Northwestern University.

bond to form the SIS microfluidic system. Mounting onto a skin-safe adhesive completes the fabrication (Fig. 2C). SIS exhibits excellent adhesion to itself and the skin adhesive without pre- or posttreatment.

Figure 2D shows a cross-sectional image of the microfluidic channel, highlighting the contoured geometry of the top surface. Here, the top layer of SIS consists of a conformal film (thickness of  $\sim 150$   $\mu\text{m}$ , with cap regions of  $\sim 80$   $\mu\text{m}$  thick). As a result, the thickness of the SIS in between the channels is smaller than the heights of the channels, thereby yielding a platform with thickness and corresponding bending stiffness that is 60 to 75% and 94 to 98% lower, respectively, than those of previously reported systems (33–35). Cutting the top, molded SIS layer to a diameter of 32 mm and the bottom layer and adhesive to a diameter of 40 mm creates a 4-mm-wide ring around the circumference that consists only of the bottom layer and adhesive. This stepwise tapered geometry creates a low-profile, conformal interface to the epidermis that also minimizes interface stresses near the edges. Figure 2E illustrates the high strain to failure ( $>2000\%$ ) and low elastic modulus ( $E = 0.83$  MPa) of SIS.

Minimizing sources of backpressure and fluidic drag is critical to allow free, unimpeded flow of sweat into the device. With a form of Poiseuille's law that accounts for capillary forces, the flow rate  $Q$  in a channel filled to a length  $L$  is given by

$$Q = whP_s \left( \frac{wh}{w+h} \right)^2 \frac{1}{8\mu L} + wh\sigma \cos \theta_A \left( \frac{wh}{w+h} \right) \frac{1}{4\mu L}$$

where  $P_s$  is the sweat pressure,  $\mu$  is the viscosity of the sweat,  $\theta_A$  is the contact angle,  $\sigma$  is the surface tension coefficient, and  $w$  and  $h$  are the width and height of the channel, respectively (38). The flow rate is proportional to the inverse of filled length  $L$ . The latter term,  $wh\sigma \cos \theta_A \left( \frac{wh}{w+h} \right) \frac{1}{4\mu L}$ , characterizes the effects of wetting of the channel.

For hydrophobic materials, where  $\theta_A > 90^\circ$ , the contribution from the capillary term is negative, thus decreasing the flow rate. Likewise, for hydrophilic materials,  $\theta_A < 90^\circ$ , this term is positive, thereby increasing flow rate. The neat contact angle of SIS is  $\sim 110^\circ$  but can be rendered hydrophilic via exposure to ozone formed by ultraviolet (UV) light (fig. S3). The flow rates of water through SIS microchannels of various sizes at a fixed pressure of 2 kPa, a physiologically relevant pressure for sweat glands (34), are summarized in Fig. 2F. Experimental details are in fig. S4. The devices shown here have channel depths of  $\sim 220$   $\mu\text{m}$  and channel widths that vary from 200  $\mu\text{m}$  (center) to 600  $\mu\text{m}$  (edge). This variation in channel width serves to maximize the areal channel footprint and thus total possible sweat capture volume, without increasing the device thickness. The 60- $\mu\text{l}$  structure fills in less than 2 min at 2 kPa, with an average flow rate of 25  $\mu\text{l}/\text{min}$  (fig. S5). Physiological sweat rates range from 12 to 120  $\mu\text{l}/\text{hour}^{-1} \text{cm}^{-2}$  (39) or from 3 to 34  $\mu\text{l}/\text{hour}$  from a collection area of  $r = 3$  mm. These designs, then, satisfy requirements for practical use. The overall results and the experimentally validated models can serve as guidelines for devices with different channel geometries.

Reliable sweat collection in aquatic settings or in arid climates requires constituent materials with excellent barrier properties to prevent



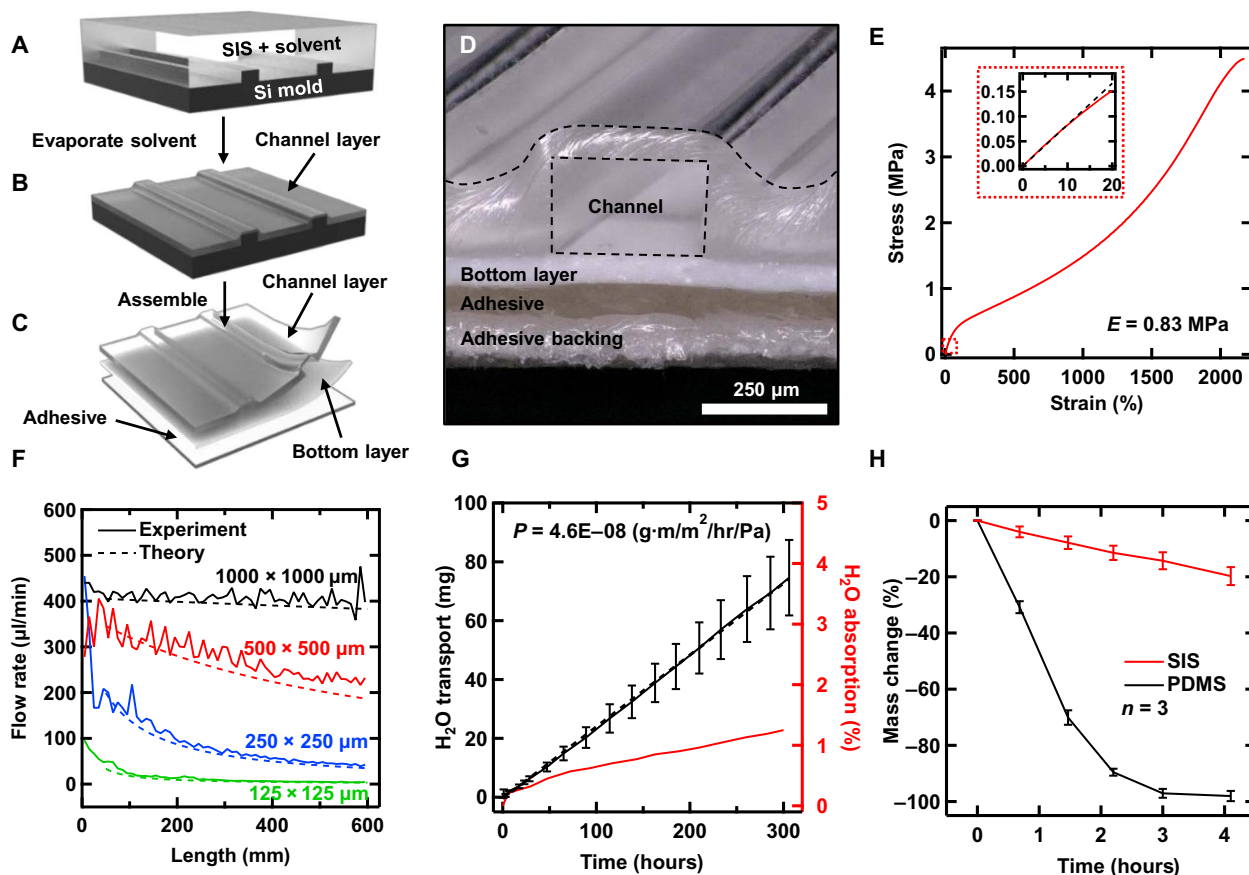


**Fig. 2. Fabrication and characterization of soft microfluidic systems constructed with SIS.** (A) SIS solvent cast on a bas-relief wafer forms a uniform coating. (B) Evaporation of the solvent leaves behind a thin layer of SIS conformal to the bas-relief. (C) The channel layer, bottom layer, and adhesive laminate together and bond via application of light pressure after demolding. (D) Cross-sectional micrograph of a microfluidic channel showing the contoured geometry of the top surface. (E) The high strain to failure (>2000%) and low elastic modulus (0.83 MPa) enable demolding of thin, delicate microfluidic structures. (F) Geometry-dependent flow rate in SIS microfluidic channels as a function of filling length for a fixed pressure of 2 kPa. (G and H) The high-barrier properties and low water uptake of SIS enable stable collection and storage of sweat in both aquatic and arid environments. Photo credit: J. Choi, Northwestern University.

contamination and to eliminate evaporative loss, respectively. Figure 2G shows results of water transport through thin membranes of SIS and of water absorption into bulk samples of SIS. Less than 80 mg of water vapor passes through a membrane of SIS with a thickness of 125  $\mu\text{m}$  and a lateral area of 1.8  $\text{cm}^2$  over 12 days in a humid (>90%) environment, corresponding to a permeability of  $4.6 \times 10^{-8} \text{ g}\cdot\text{m}/\text{mm}^2\text{/hr/Pa}$ . Bulk samples of SIS at 37°C absorb water to a mass that is less than 1.5% of its initial weight over the same time period. Comparisons of evaporative loss of water from devices constructed in SIS and in poly(dimethylsiloxane) (PDMS), the material used in previously reported systems, highlight the importance of these barrier properties for collecting and storing sweat. In particular, devices made with SIS and with open outlets can store sweat at 37°C for 4 hours with less than 20% loss, while PDMS devices of comparable geometry lose ~100% within 3 hours (Fig. 2H). Experimental details are in fig. S6. The water vapor permeability of a polymer follows Fick's laws of diffusion and is dictated largely by the bulk polymer morphology. Further improvements in resistance to water loss could be achieved by rational selection or engineering of the polymer free volume or heterogeneous integration with high-barrier materials.

### Mechanics of epidermal SIS microfluidics

Devices constructed with SIS in the geometries described previously adhere conformally to the skin and present low profiles due to the small thicknesses and tapered edges. Inducing large deformations of the skin at the location of a representative device demonstrates the degree of conformality and robustness of adhesion during extreme mechanical forces, as shown in Fig. 3A. Similar deformations with devices that do not include the tapered edge (Fig. 3B) result in delamination and peeling from the skin. Results of mechanics modeling support this observation and quantify the reductions in energy release rates for thin devices with tapered edges compared to thick devices without tapered edges (fig. S7). Figure 3 (C to F) demonstrates the response to various natural movements, as in Fig. 3G. Changes in apparent volume of the collected sweat can occur during deformations of the device due to constriction or widening of the channels. Any such changes in volume, however, reverse when the device returns to its natural state because of the high elasticity of the SIS. (fig. S8).

Finite element analysis (FEA) of stress/strain distributions and respective photographs show various mechanical distortions for a device

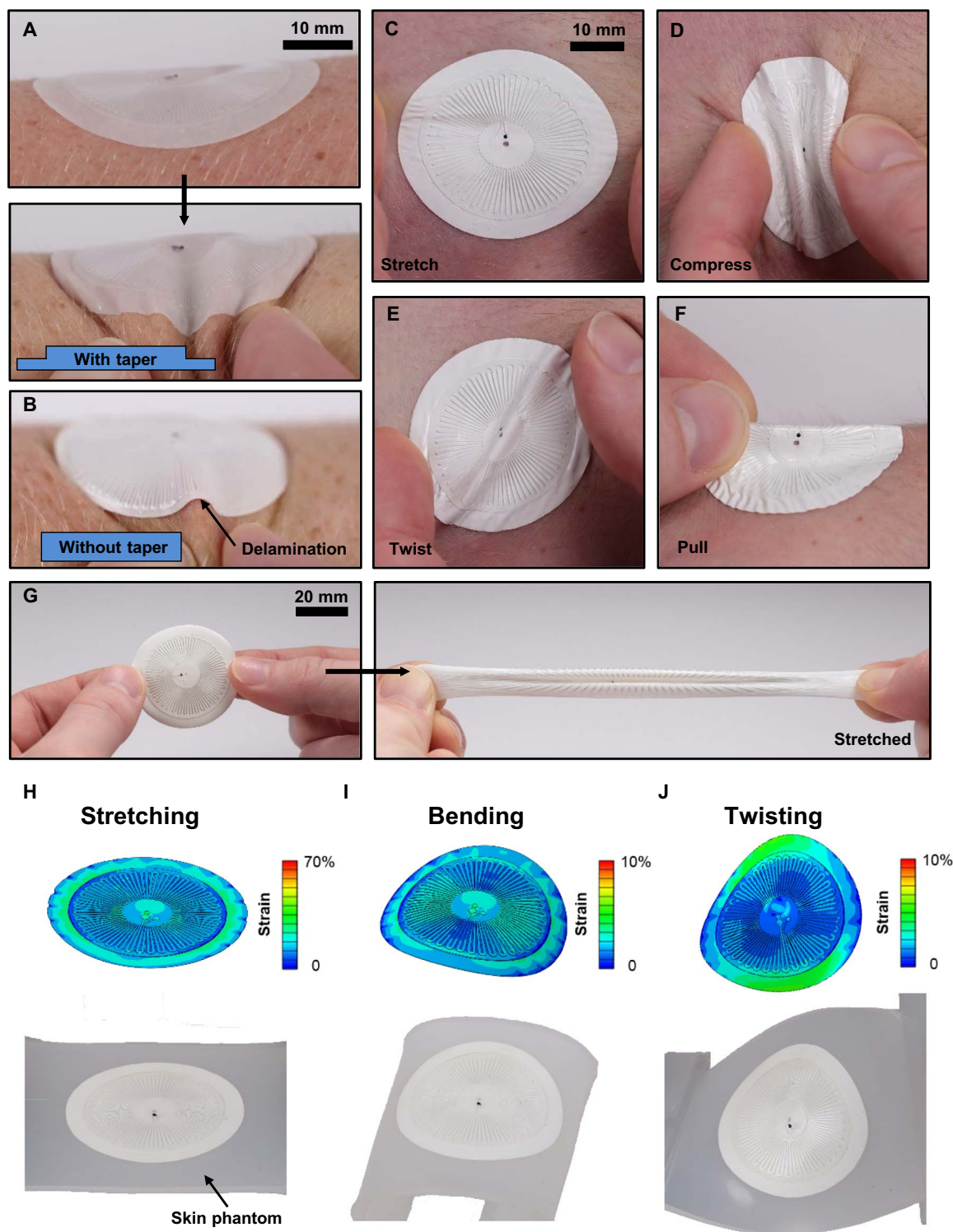


**Fig. 3. Mechanics of conformal epifluidic systems.** (A) Optical micrographs of devices with tapered edges on the skin before and after pinching to form wrinkles. (B) Delamination from the skin of a nontapered device due to wrinkling. (C) Stretched. (D) Compressed. (E) Twisted. (F) Pulled. (G) Before and after stretching to ~400%. Simulation results and experimental observations of mechanical deformations including (H) stretching (15%), (I) bending ( $r = 3$  cm), and (J) twisting (67.5°). The maximum interfacial stress is <5 kPa for all cases, which is much lower than the threshold of skin sensitivity (20 kPa). Photo credit: J. Choi, Northwestern University.

attached to a skin phantom constructed from PDMS (Fig. 3, H to J). In all deformation cases, the maximum interfacial stress between the device and skin is <5 kPa, which is much smaller than the 20 kPa

sensitivity threshold of human skin. The maximum stresses at the device/skin interface when the skin is stretched by 10% are also below the threshold for skin sensation (fig. S7E). This result suggests that the

device is imperceptible to the user during normal flexing and stretching of the skin.

### Sweat collection and biomarker detection with aquatic and dryland athletes

Optimized device structures and adhesive formulations, along with the favorable intrinsic properties of SIS, enable sweat collection in aquatic environments even during vigorous activities. Robust, underwater adhesion follows from the low profile and tapered edge of the device, as described above, and the low modulus of SIS and a strong, skin-safe adhesive. Collection of sweat from the skin without interference from an aquatic environment is enabled by the robust barrier properties of the SIS, the small diameter of the outlet port ( $r = 0.25$  mm) and the high contact angle of SIS ( $110^\circ$ ). The skin adhesive forms a watertight seal, forcing sweat from the collection area to flow into the microchannel, which displaces the air in the channel into the aquatic environment through the outlet. Water from the environment does not enter the outlet during swimming because of the small dimensions of the channels, the hydrophobicity of the SIS, and the pressure associated with air in the unfilled regions of the channels. Descending below the surface of the water generates a transient pressure differential between the trapped air in the channel and the environment due to hydrostatic pressure and is equilibrated via backfilling of pool water into the channel. The low air permeability of SIS (4 barrer,  $O_2$ ; compared to PDMS, 800 barrer,  $O_2$ ), minimizes the loss of trapped air in the channel due to pressure differentials (40, 41).

Measurements of the cumulative sweat loss, sweat rate, and chloride concentration follow from optical analysis of the microfluidic component of the system. The NFC component allows determination of skin temperature. Figure 4 (A and B) shows photographs of subjects wearing the device during swimming and biking, respectively. Here, devices are attached on the midline ventral forearm, approximately 7 cm from the tip of the elbow. A laser-patterned, skin-safe, acrylic adhesive bonds the device to the skin (referred to henceforth as the type 1 adhesive; Fig. 4C). Patterned openings reduce the area of occluded sweat glands by  $\sim 25\%$ , thereby largely eliminating compensatory effects in sweat release that would otherwise increase the local sweat rate because of occlusion of neighboring sweat glands, as observed with unpatterned adhesive layers (33, 35). Placing food dye near the device outlet enables visual observations of the extent that water backfills the device during swimming and diving (fig. S2). These results indicate that, even during intense swimming on the surface, water backfills into the channel system by an amount that is less than  $2\ \mu\text{l}$ . Thus, less than 3% of the channel is exposed to potential contamination from the environment during swimming on the surface, as this end section of the channel does not come into contact with collected sweat. Hydrostatic pressure generated from diving to 4 m can induce backfilling up to  $\sim 16\ \mu\text{l}$  or 27% of the channel volume (Fig. 4D). Upon resurfacing, 60 to 75% of this water exits back through the outlet as a result of pressure associated with air trapped in the channel. The remaining fluid remains because of capillary forces. These results serve as guidelines to inform designs that incorporate sufficient “dead” volume near the outlet to accommodate backfilling without contaminating the sweat. For designs shown here, up to  $44\ \mu\text{l}$  of sweat can be captured during aquatic activity involving diving to 4 m (corresponding to  $\sim 16\ \mu\text{l}$  of backfill) without contamination.

Concurrent measurements of local and total body sweat loss measurements via absorbent pads and changes in body weight, respectively, provide two methods of sweat loss comparison to the epifluidic de-

vice, as established in previous work (14). A comparison of sweat volume collected with patterned (type 1) and unpatterned (type 2) devices appears in fig. S9. The results indicate a higher correlation of epifluidic collection to both absorbent pad collection and percentage of body weight loss when using the type 1 adhesive pattern. Comparing data from a device with type 1 adhesive to those obtained with a foam absorbent pad and to measurements of percentage of body weight loss serves as a validation against the two most common methods for measuring local and global sweat volume loss, respectively. The epifluidic data exhibit a good correlation ( $R^2 = 0.74$ ) to results obtained with the absorbent pad for subjects who engaged in swimming and in biking (Fig. 4E). The sweat volume collected with the epifluidic device also correlates reasonably well with percentage of total body weight loss ( $R^2 = 0.63$ ; Fig. 4F). As a practical matter, reliable measurements of sweat loss from weight loss during swimming are not possible because of inadvertent, uncontrolled gain and loss of water (drinking water, urination, etc).

The performance evaluated in salt water demonstrates robust adhesion, proper filling, and operation even in extreme environments. These studies measured local sweat volume using epifluidic devices with the type 2 adhesive worn by triathletes on the ventral forearm during practice swim sessions at the IRONMAN Triathlon World Championship. Figure 4G shows representative photographs of three epifluidic devices after swimming. Additional details are in fig. S10.

The NFC electronics consist of a magnetic loop antenna, NFC chip with an on-board temperature sensor, LED, and passive components (Fig. 5A). Skin and core temperature are important because both parameters regulate sweating (42). The NFC temperature sensors built into the platforms reported here allow measurements of skin temperature of the forearm before, during, and after swimming and biking sessions (Fig. 5B). The data indicate that the skin temperature for the swimmer is initially  $\sim 32^\circ\text{C}$  and then drops to within  $1^\circ$  to  $2^\circ\text{C}$  of the temperature of the pool water ( $26^\circ\text{C}$ ) soon after entering the water. The temperature rises slightly after swimming for 20 min ( $\sim 1000$  m) but remains within  $2^\circ\text{C}$  of that of the pool. The skin returns to the initial temperature within 10 min of exiting the pool and drying off. The skin temperature of the biking subject initially drops as the result of vasoconstriction (43) and subsequently increases to  $\sim 1.2^\circ\text{C}$  above the initial baseline. The presence of the device inhibits sweat evaporation at the mounting location, thereby leading to increases in temperature of  $\sim 1^\circ\text{C}$  relative to the temperature of adjacent regions of the skin (fig. S11). Adding microperforations to the device facilitates sweat evaporation and eliminates this temperature increase.

Quantitative measurement of biomarkers in sweat collected in aquatic settings is possible by limiting the backfilling and thus contamination. As described previously, swimming on the surface can lead to filling of the last  $2\ \mu\text{l}$  of the channel adjacent to the outlet with water from the environment. This water is not ejected but does not contact collected sweat for volumes less than  $58\ \mu\text{l}$ . The chloride ion assay uses a reagent that changes color by an amount that quantitatively depends on chloride concentration. A fixed, printed color reference dial facilitates visual readout. The color reference dial was constructed from  $a^*$  and  $b^*$  color values obtained from the reaction of stock chloride solutions of known concentration with the reagent in an epifluidic device (Fig. 5C). The  $a^*$  and  $b^*$  color values correspond to projections onto the  $a^*$  and  $b^*$  coordinate axes which, along with a coordinate axis for lightness ( $L^*$ ), form the basis of the  $L^*a^*b^*$  color space. In field trials, subjects wore devices containing the chloride assay on the ventral forearm along with a reference SIS epifluidic device without the



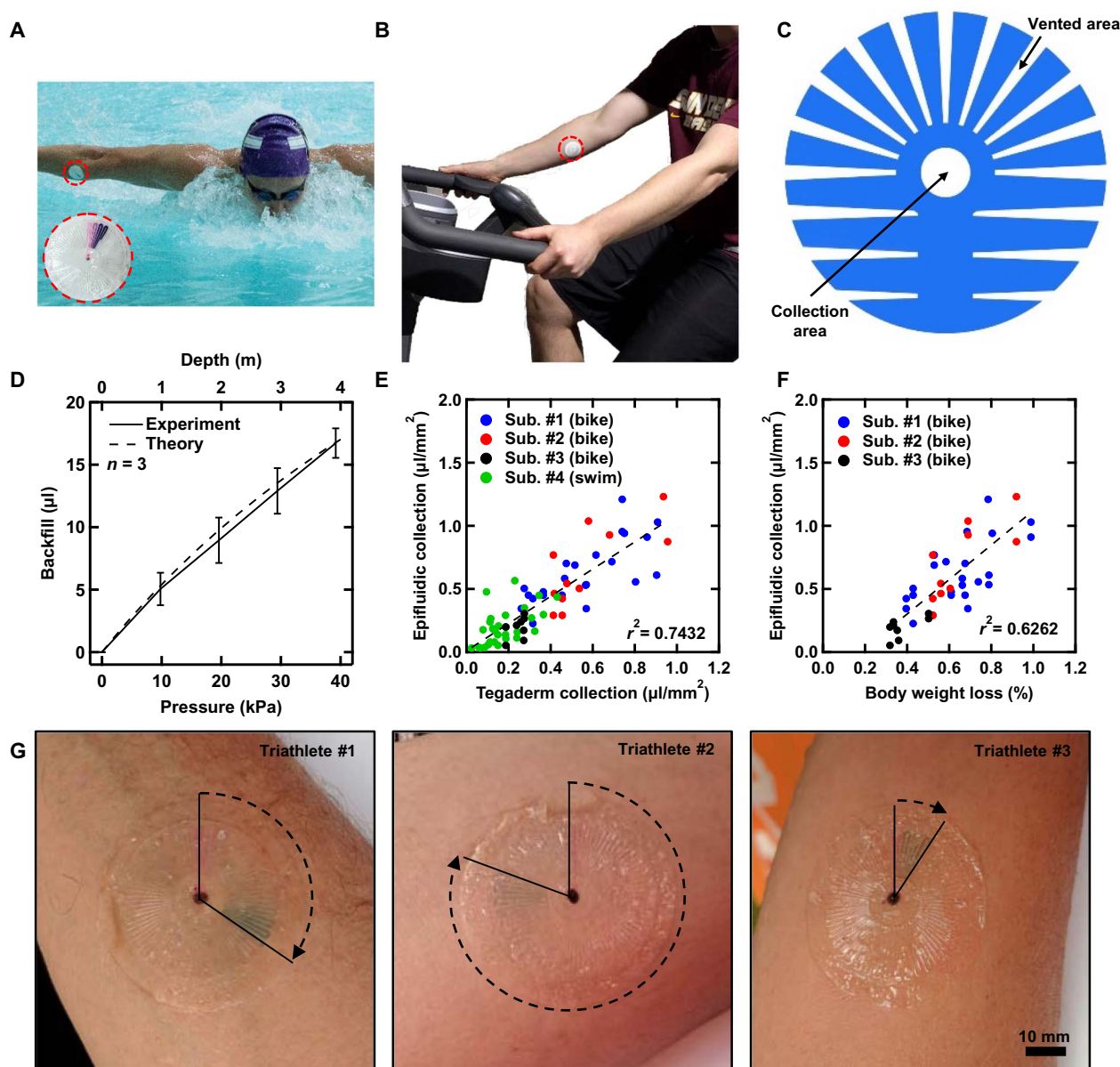


**Fig. 4. Sweat collection from aquatic and dryland athletes.** (A) A subject wearing an epifluidic device during a swimming study. (B) A subject wearing an epifluidic device during a biking study. (C) The sweat collection area, defined by the geometry of the adhesive layer, is a circle with  $r = 3$  mm. Vents, corresponding to regions without the adhesive, extend radially from the center to reduce the number of occluded sweat glands and, thereby, to minimize the effects of compensatory sweating. (D) Experimental and theoretical (ideal gas law) data on backfilling of a device after submerging at various depths. (E) A good correlation exists between the sweat volume per area collected via the epifluidic devices and that obtained with an absorbent pad as a result of biking and swimming exercises. (F) A good correlation between the sweat volume per area collected via the epifluidic devices and the percentage of body weight loss as a result of biking exercise. (G) Representative images of epifluidic devices on three IRONMAN triathletes after exercising. Photo credit: (A) J. T. Reeder and (B) J. Choi, Northwestern University, and (G) K. Barnes, Gatorade Sports Science Institute.

reagent to allow capture of sweat for ex situ analysis with a chloridometer. Devices were imaged after subjects swam for 45 min (~2500 m) or biked for 30 min (~14 km) to collect at least 15  $\mu$ l of sweat in the reference device. Results from four subjects are shown in Fig. 5D, along with reference chloride values measured using a chloridometer. The chloride concentration of the pool water was 18 mM. LAB color values extracted from images of the devices after correcting for offsets in white balance appear as a function of the reference chloride values in Fig. 5E. The calibration curve shown in the same graph indicates the ability to measure chloride levels with an accuracy of  $\pm 10$  mM.

The LAB value plotted in Fig. 5E corresponds to the magnitude of the measured  $\mathbf{a}^*\mathbf{b}^*$  vector as projected on to the calibration vector in Fig. 5C. Colorimetric measurements of chloride concentration with improved accuracy are possible with optimized microchannel geometries and color extraction algorithms (14, 33).

The conformal mechanics and water barrier properties of SIS epifluidics enable sweat collection from unconventional mounting locations and over long durations, which has potential for enabling new noninvasive clinical diagnostics. Conformal adhesion enables sweat rate comparisons after a 15-min sauna test from a highly deformable,

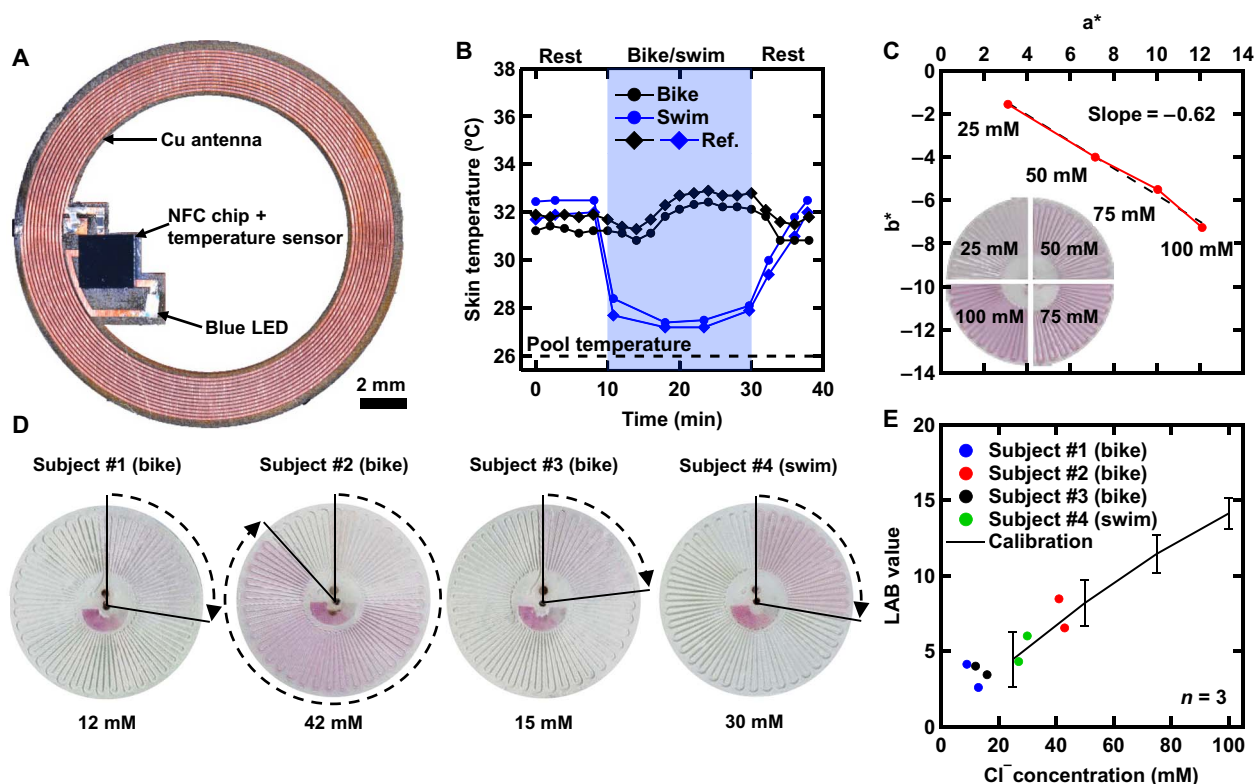


**Fig. 5. Digital thermography and chloride sensing.** (A) The NFC electronics consist of a magnetic loop antenna, NFC chip with an on-board temperature sensor, LED, and passive components. (B) Skin temperature measurements during 20-min sessions of swimming and biking elucidate effects of the environment, perfusion, and sweat generation. (C) The  $a^*$  and  $b^*$  color values associated with reference chloride solutions after reacting with silver chloranilate. Inset: Photographs of SIS devices with a silver chloranilate reagent after reacting with reference chloride solutions. (D) Images of devices used for measuring chloride concentrations in sweat generated by swimming and biking. (E) LAB color values from the colorimetric reagent for chloride measurements compared to results obtained with a chloridometer.

curved, and wrinkled skin without discomfort, including the side of the neck (20  $\mu$ l; Fig. 6A), armpit (4.5  $\mu$ l; Fig. 6B), and forehead (19.5  $\mu$ l; Fig. 6C). Sweat from the armpit is secreted from both eccrine and apocrine glands, the latter of which contains pheromones and proteins, which could provide physiological insights not accessible via eccrine sweat. Sweat collection from mechanically dynamic areas such as the armpit is traditionally difficult because of delamination, and conventional techniques require ex situ processing, which precludes real-time diagnostics of apocrine sweat. An assessment of the difference in bilateral sweat rate on the forehead has been shown to be a promising method for evaluating the autonomic dysfunction of patients with stroke (44). This platform is also suitable for vulnerable populations such as on the soft, delicate skin of a baby during a bath (Fig. 6D). Newborns regularly undergo sweat tests for screening of cystic fibrosis, which is detected by measuring the chloride concentration of the sweat. Conventional devices are rigid and attached to the skin with straps, presenting a compelling opportunity for improved methods of in situ screening using soft epifluidics (45). The high-barrier properties of SIS and thus low rate of sweat evaporation enable collection during sedentary periods in a warm environment over 8 hours (Fig. 6E). This capability creates opportunities for long-duration sweat collection and analysis from nonambulatory patient populations, where physical exercise is unfeasible, such as for monitoring recovery of patients with stroke via differing bilateral sweat rates (44), testing for drug metabolites in sweat (46), screening for diabetes via sweat glucose (47), and providing insights into kidney disease via urea and creatinine in the sweat (48).

## DISCUSSION

This paper establishes soft, waterproof materials, design considerations, and device architectures for skin-integrated systems capable of real-time monitoring of the fluid loss and electrolyte concentration of aquatic athletes via measurements of local sweat rate, sweat loss, colorimetric analysis of chloride concentration, and digital measurements of skin temperature. The use of a soft, elastomeric styrenic block copolymer (SIS) for the microfluidic system and for encapsulating the electronics represents an enabling feature due to its attractive combination of mechanical properties and barrier characteristics. Quantitative studies of these materials and various properties of sweat transport through microchannels of SIS establish the advanced utility of epifluidic systems in aquatic and/or arid environments. Experimentally validated models of flow and mechanics, as well as field studies, collectively demonstrate the seamless operation of sweat collection from aquatic athletes without interference from pool or ocean water. Robust and watertight bonding to the skin, even under extreme conditions of underwater operation for extended periods of time (>2 hours), follows from optimized device construction, ultrathin edge geometries, and use of strong, skin-safe adhesives. These results highlight advanced capabilities in real-time physiological measurements on swimmers and dryland athletes alike. The principles and device designs will be useful for robust epidermal sweat collection and analysis systems in these and other extreme environments, with consequences not only in athletic performance and fitness but also in military readiness and clinical medicine. A next step in this line of research is to explore the



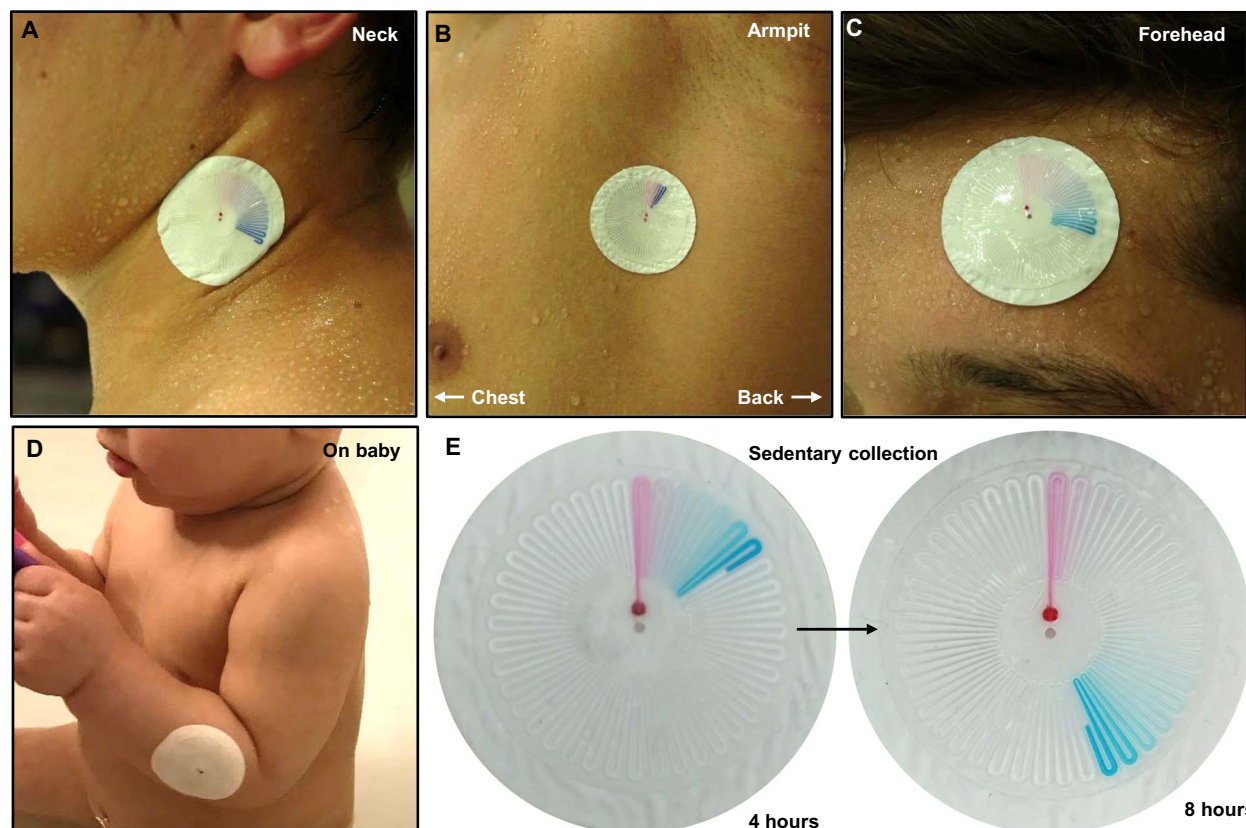


**Fig. 6. Sweat collection in unconventional scenarios.** Thin, conformal mechanics associated with devices introduced here enable sweat collection under high levels of deformation and from unusual locations including the (A) neck, (B) armpit, and (C) forehead. (D) Soft, thin device construction enables conformation to delicate skin, such as that of a baby during a warm bath. (E) High-barrier properties of the SIS enable reliable collection of sweat at low rates ( $<4 \mu\text{l}/\text{hour}$ ) over 8 hours from the lower back of a sedentary subject. Photo credit: (A to C) J. T. Reeder and (D) S. Xu, Northwestern University.

physiology of aquatic sweating using this materials platform. For example, the local sweat loss and composition vary substantially across the body based on intra- and interindividual factors such as mounting location, environment, and physique (49, 50). Expanded studies will help to verify the relation between local sweat via the epifluidic device versus whole-body sweat fluid electrolyte losses during aquatic exercise to establish its utility in informing hydration recommendations.

## MATERIALS AND METHODS

### Fabrication of ultrathin SIS microfluidic systems

Spin coating a 10- $\mu\text{m}$ -thick layer of negative photoresist (KMPR 1010) at 3000 rpm and at 1000 rpm/s for 30 s and soft baking at 110°C for 5 min prepared a silicon wafer for patterning. Exposure to UV light (420 mJ/cm<sup>2</sup>) through an iron oxide mask transferred the pattern into the photoresist. The wafer was hard baked at 110°C for 5 min and developed in AZ 917MIF for 3 min. Deep reactive ion etch created trenches in the silicon wafer to a depth of 250  $\mu\text{m}$  (STS Pegasus ICP-DRIE, SPTS Technologies Ltd.). Exposure to oxygen plasma (200 W, 200 mT; March CS-1701) for 15 min stripped the remaining photoresist. A fluorinated silane [trichloro(1H,1H,2H,2H-perfluorooctyl) silane, Sigma-Aldrich] vapor deposited onto the patterned wafer by placing it in a vacuum desiccator with 20  $\mu\text{l}$  of the silane for 12 hours formed a nonadhesive layer on the exposed silicon surfaces. Rinsing

with isopropyl alcohol removed residual silane. Patterned and flat wafers underwent the same silane deposition process.

Dissolving 15 g of poly(styrene-isoprene-styrene) (14% styrene; Sigma-Aldrich) in 100 ml of propyl acetate (Alfa Aesar), with shaking periodically over a 24-hour period to ensure full dissolution, formed a solution for casting against a patterned silicon wafer. Mixing 2 weight % (wt %) titanium dioxide powder (Sigma-Aldrich) with the SIS solution and mixing in a planetary mixer (Thinky ARE-310) for 4 min at 2000 rpm yielded an opaque, white color. A poly(tetrafluoroethylene)-coated metal ring (Norpro 666) placed on the silanized, patterned wafer served to contain the solution at the edges. An 8-g sample of clear SIS solution formed the top, patterned layer. A 6-g sample of white SIS solution formed the bottom layer. Subsequent vacuum desiccation for 12 hours served two purposes: (i) to remove bubbles and (ii) to provide a slow evaporation rate by maintaining a vapor bath around the SIS solution. The samples were dry to the touch after 12 hours. Heating for 6 hours at 80°C on a hot plate removed any remaining solvent. Light pressing and waiting at 30 min was sufficient to form permanent, watertight bonds between the SIS layers and the adhesive.

### Fabrication of flexible NFC circuits and magnetic loop antennas

Laser structuring of a copper laminate (Pyralux AP8535R) by means of ablation (LPKF U4) formed flexible printed circuit boards (PCBs)

for the NFC systems. Sonication in stainless steel flux, deionized (DI) water, and IPA prepared the PCBs for mounting of active (AMS SL13A) and passive components [resistors, capacitors in 0201 package, and blue LED (OSRAM 720-LBVH9GN1P2351Z) in 0402 package] using low-temperature solder paste and a heat gun. Measurement of the resonant frequency of the NFC part of the circuit using a passive method (Keysight E4990A) confirmed the matched capacitance of the antenna and NFC chip, with adjustments as necessary via replacement of passive components. Dip coating the completed device in a solution of SIS in propyl acetate (5 wt %) three times with a 30-s drying step in between coats formed a waterproof encapsulation.

### Processes for assembling the devices

A circular steel punch ( $d = 32$  mm) and 0.5-mm steel punch defined the outer diameter and the outlet port for the molded SIS sheet, respectively. A 0.5- $\mu$ l volume of colorimetric agent (food dye or silver chloranilate solution) filled the reaction chamber of the device. Americolor Soft Gel Paste, Violet, served as the food dye. The silver chloranilate solution consisted of 0.1 g of silver chloranilate (City Chemical) in 0.5 ml of 1 wt % aqueous poly(acrylic acid) (Sigma-Aldrich). Vortexing this solution before application to the patterned, top layer ensured good dispersion. A CO<sub>2</sub> laser cutting system (Universal Laser Systems VLS3.50) formed the necessary patterns in a uniform sheet of skin adhesive (Scapa Unifilm U884). The white, bottom layer of SIS and the laser-patterned adhesive encapsulated the SIS-coated NFC coil on the top and bottom, respectively. A 1-mm-diameter steel punch created a hole for the inlet in the white SIS. Applying a color reference dial to the white SIS layer adjacent to the inlet facilitated direct colorimetric readout of the chloride level in the sweat with the naked eye or with cell phone camera and digital image processing. Lamination of the molded SIS layer with the reagent onto the flat, white layer of SIS encapsulated the color reference dial and reagent. Cutting the edges with a steel punch ( $d = 40$  mm) defined the outer perimeter of the device. Lightly pressing on the assembly and waiting for 30 min yielded a watertight bond between the microfluidic device layers.

### Measurements of contact angle

Exposure of a sample of SIS to UV ozone (UVO; Jelight Model 144A) oxidized the surface. Each sample was prepared in triplicate. A VCA Optima XE contact angle measurement system enabled measurement of the evolution of the contact angle associated with 0.5- $\mu$ l droplets of DI water.

### Characterization of the mechanical properties

Tensile testing (MTS Sintech 20G) of samples of SIS in dogbone geometries (ASTM D1708) yielded the stress/strain relationships across a range of strains from 0 to 2000%. A line fit between 0 and 10% strain yielded the Young's modulus. The strain rate was 20 mm/min.

### Measurements of flow rates in microfluidic test structures

Tests of flow rate used molded SIS microfluidic structures with 61-cm-long channels of various cross sections ( $125 \times 125$ ,  $250 \times 250$ ,  $500 \times 500$ , and  $1000 \times 1000$   $\mu$ m). Aluminum structures (6061) machined using a three-axis mill (Roland MDX-540) served as the molds. Vacuum desiccation for 30 min removed bubbles from SIS cast in these molds and subsequently dried on a hot plate at 80°C for 5 hour. A steel punch formed inlet and outlet holes (1 mm), and the molded layer was bonded to a flat SIS layer by light pressing. Mounting the sample to a

Plexiglas holder with the device inlet aligned to a 2-mm aperture in the holder prepared the device for filling. A pressure-driven flow controller (Fluigent MFCS-EZ) pumped DI water at 2 kPa through the aperture and into the device. A camera (Canon EOS Rebel T6i) placed above the device recorded the progression of the fluid through the channel. Extracting time points from the recorded video when the front of the flow passed 10-mm increments yielded the flow rate for each sample.

### Measurements of water vapor penetration and absorption

Measurements of water vapor penetration and water adsorption followed the ASTM E96 and D860 protocols, respectively. Measuring the change in weight of a 20-ml scintillation vial filled with a desiccant and covered with a sheet of SIS yielded data on the rate of water vapor transmission. A 150- $\mu$ m-thick sheet of SIS sealed the mouth of the vial. Placing the vial and SIS sample in a sealed container with an open petri dish of water inside allowed testing in a humid environment. The humidity inside the sealed container was >95%, and temperature was 20° to 25°C. Recording the increase in the mass of the vial periodically using a microbalance (Mettler ML204T) yielded the permeability of the SIS. Measuring the change in weight of puck-shaped pieces of SIS submerged in DI water yielded data on the rate of water absorption. A capped, scintillation vial filled with DI water and stored in an oven at 37°C formed an aqueous environment for the pucks ( $d$ , 4 cm; thickness, 2 mm). The samples were periodically removed from the vial, gently dried using a lint-free wipe, and weighed on a microbalance.

Filling SIS and PDMS devices with water and placing them in an arid environment (37°C; relative humidity, <10%) yielded data on the rate of evaporative water loss. A double-sided adhesive bonded the devices to a glass slide and ensured that evaporative water loss occurred through only the top of the device. Each sample was weighed every hour using a microbalance. Tests were performed in triplicate.

### Measurements of sweat loss in human field studies

The experimental protocol for the dryland and pool studies was approved by the Institutional Review Board of Northwestern University (STU00207078), and all subjects gave written informed consent before participation. The experimental protocol for the Kona IRONMAN Triathlon was approved by the Sterling Institutional Review Board. All subjects consented to their images being taken as detailed in the protocols of the Northwestern and Sterling Institutional Review Boards. Imaging devices used for Northwestern sweat volume trials with a smart phone (LG Nexus 5X) recorded the device status within 5 min of finishing the exercise. Collected sweat volume was determined by counting the number of completed serpentine to the nearest half serpentine ( $\pm 0.75$   $\mu$ l). Measurements of percentage of body weight loss (total body loss) and mass gain of skin-mounted absorbent foam pads (local loss) provided two methods of comparison to the volume collected in the SIS epifluidic device. A body weight scale with 4-g precision (Adams GFK 330ah) enabled high-precision measurements of percentage of body weight loss before and after exercise while wearing either a swimsuit or underwear. The animal (dynamic) measurement mode was used, which filters variations resulting from movement during the weighing procedure. Body weight measurements for the Kona IRONMAN Triathlon trials were performed in the nude after a 5-min warm up and after swimming using a Tanita scale with 10-g precision. Cleaning the application sites with an IPA wipe removed residual salts/oils and ensured good adhesion of the

device. A rosin skin pretreatment (Gordon Labs, Stik-It) enhanced underwater adhesion during the Kona trials. Applying the pretreatment only to the skin underneath the adhesive prevented the inhibition of the sweat glands in the collection area. After applying to the skin, pressure was applied for 10 s to ensure good adhesion. Absorbent foam pads (3M Tegaderm 3582) mounted nearby the SIS devices recorded local sweat loss. Weighing the absorbent pads immediately following the workout using a microbalance (Vibra 224R) produced the wet weight. Placing the pads in a 50°C oven for 24 hours evaporated the water before weighing again (dry weight). Weight due to skin oils, salt content, etc was assumed to be negligible. Subtracting the dry weight from the wet weight and dividing by the area of the absorbent pad (1000 mm<sup>2</sup>) yielded the local sweat loss. Calibration and reference chloride measurements were performed on a Chloro-Chek Chloridometer with a coefficient of variation of 1.02% at 100 mM. No skin irritation due to the epifluidic device or the absorbent pad was observed during the trials.

### Measurements of skin temperature in human field studies

The on-board temperature sensor of the AMS SL13A NFC chip enabled wireless skin temperature measurements. The AMS SL13A demo application on an LG Nexus 5X cell phone enabled untethered pairing and readout of the skin temperature. An infrared camera served as the reference temperature measurement (FLIR A655sc) for the biking experiments and a handheld thermocouple reader (type-k) for the swimming trial. Recording skin temperature measurements every 500 m during swim trials yielded the time evolution of the skin temperature. Quickly drying the measurement area with a towel before the NFC and reference measurements avoided spurious results due to water evaporation. Less than 15 s passed in between the swimmer, reaching the pool wall and the measurements being taken. Laser drilling (Universal Laser Systems VLS3.50) 125- $\mu$ m-diameter holes with a 250- $\mu$ m pitch across a 40-mm-diameter SIS/adhesive sheet yielded the perforated device.

### Procedures for calibrating the chloride assay

Filling epifluidic devices containing the silver chloranilate reagent with 20  $\mu$ l of known sodium chloride concentrations (25, 50, 75, and 100 mM) produced the reference color values for calibrating the chloride measurement. Imaging of the resulting product using a Canon EOS Rebel T6i DSLR camera with auxiliary LED lighting yielded the reference images. LAB color values were extracted from the images after correcting the white balance using a color checker (SpyderCheckr 24). The LAB color values from the images of the 25, 50, 75, and 100 mM concentrations formed the reference dial. Printing the reference dial on a 25- $\mu$ m-thick polyester sheet with adhesive backing (FLEXCon THERMLfilm SELECT 10852) using a commercial ink-jet printer enabled lamination onto the device. Verification of the reference colors was performed by repeating the calibration while using the color reference dial instead of correcting for white balance.

### Measurements of sweat chloride levels in human field studies

Devices containing the silver chloranilate reagent and an empty reference device were mounted on the midline of ventral forearm approximately 1 cm apart. Subjects swam for 45 min (~2500 m) or biked for 30 min (~14 km), and at least 15  $\mu$ l of sweat was collected in the reference device. Imaging of devices within 5 min of finishing the

exercise using a Canon EOS Rebel T6i DSLR camera enabled extraction of the LAB color values in Photoshop. Converting the a\* and b\* color values using the calibration curve produced the chloride concentration measurement.

### FEA of the device under various mechanical loadings

Full three-dimensional (3D) FEA was used to study the mechanical performance of the devices, which were mounted on phantom skin (Ecoflex, 60kPa, 60 by 60 by 2.5 mm) and subjected to stretching, bending, and twisting. For stretching, displacements corresponding to 30% stretching were applied to two ends of the skin, which resulted in an ~20% average tensile stretch on the bottom surface of the device along the stretching direction. For twisting, the two ends of the skin are twisted by 67.5° relatively. For bending, the bottom surface of the phantom skin was pressed to a rigid cylinder of 3-cm radius. Eight-node 3D solid elements were used for SIS microfluidic channels, adhesive layer, and phantom skin.

### FEA of energy release rate during biaxial stretching

The energy release rate is the energy dissipated during fracture per unit of newly created fracture surface area, which quantifies the driving force of fracture. Crack propagation occurs when the energy release rate reaches a critical value. FEA was used to calculate the energy release at the adhesive/skin interface when the device was subjected to biaxial stretching. An axisymmetric model was adopted, with the four-node axisymmetric element CAX4R for the SIS microfluidic channels, adhesive layer, and phantom skin. J integral was used to calculate the energy release rate. Modeling results for three different cases (thin SIS devices with and without taper and thick SIS device without taper) revealed that the tapered structure and reduction of the overall thickness of the microfluidic channel effectively reduce the induced energy during stretching, which helped to avoid potential delamination.

### SUPPLEMENTARY MATERIALS

Supplementary material for this article is available at <http://advances.sciencemag.org/cgi/content/full/5/1/eaau6356/DC1>

- Fig. S1. NFC coil components.
- Fig. S2. Environmental backfilling due to hydrostatic pressure and impact.
- Fig. S3. Aging of SIS rendered hydrophilic by UVO treatment.
- Fig. S4. Setup for measuring flow rates through SIS-based microfluidic systems.
- Fig. S5. Filling rates at physiological pressures.
- Fig. S6. Experimental setup for comparison of evaporation rate of sweat after collection.
- Fig. S7. Mechanical effect of tapered edge and SIS thickness.
- Fig. S8. Effect of deformation on apparent sweat volume.
- Fig. S9. Impact of adhesive geometry on sweat collection.
- Fig. S10. Details for the trial with IRONMAN triathletes.
- Fig. S11. Influence of epidermal sweat device on heat and sweat generation during biking.

### REFERENCES AND NOTES

1. S. Emaminejad, W. Gao, E. Wu, Z. A. Davies, H. Y. Y. Nyein, S. Challa, S. P. Ryan, H. M. Fahad, K. Chen, Z. Shahpar, S. Talebi, C. Milla, A. Javey, R. W. Davis, Autonomous sweat extraction and analysis applied to cystic fibrosis and glucose monitoring using a fully integrated wearable platform. *Proc. Natl. Acad. Sci. U.S.A.* **114**, 4625–4630 (2017).
2. S. S. Gambhir, T. J. Ge, O. Vermesh, R. Spitler, Toward achieving precision health. *Sci. Transl. Med.* **10**, eaao3612 (2018).
3. A. J. Bandothkar, V. W. S. Hung, W. Jia, G. Valdés-Ramírez, J. R. Windmiller, A. G. Martínez, J. Ramírez, G. Chan, K. Kerman, J. Wang, Tattoo-based potentiometric ion-selective sensors for epidermal pH monitoring. *Analyst* **138**, 123–128 (2013).



4. J. Kim, W. R. de Araujo, I. A. Samek, A. J. Bandonkar, W. Jia, B. Brunetti, T. R. L. C. Paixão, J. Wang, Wearable temporary tattoo sensor for real-time trace metal monitoring in human sweat. *Electrochem. Commun.* **51**, 41–45 (2015).
5. W. Gao, S. Emaminejad, H. Y. Y. Nyein, S. Challa, K. Chen, A. Peck, H. M. Fahad, H. Ota, H. Shiraki, D. Kiriya, D.-H. Lien, G. A. Brooks, R. W. Davis, A. Javey, Fully integrated wearable sensor arrays for multiplexed in situ perspiration analysis. *Nature* **529**, 509–514 (2016).
6. S. Imani, A. J. Bandonkar, A. M. V. Mohan, R. Kumar, S. Yu, J. Wang, P. P. Mercier, A wearable chemical–electrophysiological hybrid biosensing system for real-time health and fitness monitoring. *Nat. Commun.* **7**, 11650 (2016).
7. H. Lee, C. Song, Y. S. Hong, M. S. Kim, H. R. Cho, T. Kang, K. Shin, S. H. Choi, T. Hyeon, D.-H. Kim, Wearable/disposable sweat-based glucose monitoring device with multistage transdermal drug delivery module. *Sci. Adv.* **3**, e1601314 (2017).
8. X. Huang, Y. Liu, K. Chen, W.-J. Shin, C.-J. Lu, G.-W. Kong, D. Patnaik, S.-H. Lee, J. F. Cortes, J. A. Rogers, Stretchable, wireless sensors and functional substrates for epidermal characterization of sweat. *Small* **10**, 3083–3090 (2014).
9. D. P. Rose, M. E. Ratterman, J. C. Griffin, L. Hou, N. Kelley-Loughnane, R. R. Naik, J. A. Hagen, I. Papautsky, J. C. Heikenfeld, Adhesive RFID sensor patch for monitoring of sweat electrolytes. *IEEE Trans. Biomed. Eng.* **62**, 1457–1465 (2015).
10. P. Mostafalu, M. Akbari, K. A. Alberti, Q. Xu, A. Khademhosseini, S. R. Sonkusale, A toolkit of thread-based microfluidics, sensors, and electronics for 3D tissue embedding for medical diagnostics. *Microsyst. Nanoeng.* **2**, 16039 (2016).
11. A. K. Yetisen, M. S. Akram, C. R. Lowe, Paper-based microfluidic point-of-care diagnostic devices. *Lab Chip* **13**, 2210–2251 (2013).
12. S. Patel, H. Park, P. Bonato, L. Chan, M. Rodgers, A review of wearable sensors and systems with application in rehabilitation. *J. Neuroeng. Rehabil.* **9**, 21 (2012).
13. A. Pantelopoulou, N. G. Bourbakis, A survey on wearable sensor-based systems for health monitoring and prognosis. *IEEE Trans. Syst. Man Cybern. Part C* **40**, 1–12 (2010).
14. J. Choi, R. Ghaffari, L. B. Baker, J. A. Rogers, Skin-interfaced systems for sweat collection and analytics. *Sci. Adv.* **4**, eaar3921 (2018).
15. M. Bariya, H. Y. Y. Nyein, A. Javey, Wearable sweat sensors. *Nat. Electron.* **1**, 160–171 (2018).
16. L. B. Baker, K. A. Barnes, M. L. Anderson, D. H. Passe, J. R. Stofan, Normative data for regional sweat sodium concentration and whole-body sweating rate in athletes. *J. Sports Sci.* **34**, 358–368 (2016).
17. J. E. Greenleaf, Problem: Thirst, drinking behavior, and involuntary dehydration. *Med. Sci. Sports Exerc.* **24**, 645–656 (1992).
18. G. R. Cox, E. M. Broad, M. D. Riley, L. M. Burke, Body mass changes and voluntary fluid intakes of elite level water polo players and swimmers. *J. Sci. Med. Sport* **5**, 183–193 (2002).
19. F. Macaluso, V. Di Felice, G. Boscaio, G. Bonsignore, T. Stampone, F. Farina, G. Morici, Effects of three different water temperatures on dehydration in competitive swimmers. *Sci. Sports* **26**, 265–271 (2011).
20. R. J. Maughan, L. A. Dargavel, R. Hares, S. M. Shirreffs, Water and salt balance of well-trained swimmers in training. *Int. J. Sport Nutr. Exerc. Metab.* **19**, 598–606 (2009).
21. R. Soler, M. Echegaray, M. A. Rivera, Thermal responses and body fluid balance of competitive male swimmers during a training session. *J. Strength Cond. Res.* **17**, 362–367 (2003).
22. R. G. McMurray, S. M. Horvath, Thermoregulation in swimmers and runners. *J. Appl. Physiol.* **46**, 1086–1092 (1979).
23. T. Hew-Butler, M. H. Rosner, S. Fowkes-Godek, J. P. Dugas, M. D. Hoffman, D. P. Lewis, R. J. Maughan, K. C. Miller, S. J. Montain, N. J. Rehrer, W. O. Roberts, I. R. Rogers, A. J. Siegel, K. J. Stumpfle, J. M. Winger, J. G. Verbalis, Statement of the 3rd International Exercise-Associated Hyponatremia Consensus Development Conference, Carlsbad, California, 2015. *Br. J. Sports Med.* **49**, 1432–1446 (2015).
24. B. Lara, C. Gallo-Salazar, C. Puente, F. Areces, J. J. Salinero, J. Del Coso, Interindividual variability in sweat electrolyte concentration in marathoners. *J. Int. Soc. Sports Nutr.* **13**, 31 (2016).
25. R. S. Cairns, T. Hew-Butler, Incidence of exercise-associated hyponatremia and its association with nonosmotic stimuli of arginine vasopressin in the GNW100s ultra-endurance marathon. *Clin. J. Sport Med.* **25**, 347–354 (2015).
26. W. D. B. Hiller, M. L. O'Toole, E. E. Fortess, R. H. Laird, P. C. Imbert, T. D. Sisk, Medical and physiological considerations in triathlons. *Am. J. Sports Med.* **15**, 164–167 (1987).
27. S. Wagner, B. Knechtle, P. Knechtle, C. A. Rüst, T. Rosemann, Higher prevalence of exercise-associated hyponatremia in female than in male open-water ultra-endurance swimmers: The 'Marathon-Swim'in Lake Zurich. *Eur. J. Appl. Physiol.* **112**, 1095–1106 (2012).
28. D. J. Casa, P. M. Clarkson, W. O. Roberts, American College of Sports Medicine roundtable on hydration and physical activity: Consensus statements. *Curr. Sports Med. Rep.* **4**, 115–127 (2005).
29. American College of Sports Medicine, M. Sawka, L. M. Burke, E. R. Eichner, R. J. Maughan, S. J. Montain, N. S. Stachenfeld, American College of Sports Medicine position stand. Exercise and fluid replacement. *Med. Sci. Sports Exerc.* **39**, 377–390 (2007).
30. K. Buettner, Diffusion of water and water vapor through human skin. *J. Appl. Physiol.* **6**, 229–242 (1953).
31. S. N. Cheuvront, R. W. Kenefick, CORP: Improving the status quo for measuring whole body sweat losses. *J. Appl. Physiol.* **123**, 632–636 (2017).
32. Y. Epstein, W. O. Roberts, The pathophysiology of heat stroke: An integrative view of the final common pathway. *Scand. J. Med. Sci. Sports* **21**, 742–748 (2011).
33. A. Koh, D. Kang, Y. Xue, S. Lee, R. M. Pielak, J. Kim, T. Hwang, S. Min, A. Banks, P. Bastien, M. C. Manco, L. Wang, K. R. Ammann, K.-I. Jang, P. Won, S. Han, R. Ghaffari, U. Paik, M. J. Slepian, G. Balooch, Y. Huang, J. A. Rogers, A soft, wearable microfluidic device for the capture, storage, and colorimetric sensing of sweat. *Sci. Transl. Med.* **8**, 366ra165 (2016).
34. J. Choi, Y. Xue, W. Xia, T. Ray, J. T. Reeder, A. J. Bandonkar, D. Kang, S. Xu, Y. Huang, J. A. Rogers, Soft, skin-mounted microfluidic systems for measuring secretory fluidic pressures generated at the surface of the skin by eccrine sweat glands. *Lab Chip* **17**, 2572–2580 (2017).
35. J. Choi, D. Kang, S. Han, S. B. Kim, J. A. Rogers, Thin, soft, skin-mounted microfluidic networks with capillary bursting valves for chrono-sampling of sweat. *Adv. Healthc. Mater.* **6**, 1601355 (2017).
36. D.-H. Kim, N. Lu, R. Ma, Y.-S. Kim, R.-H. Kim, S. Wang, J. Wu, S. M. Won, H. Tao, A. Islam, K. J. Yu, T.-i. Kim, R. Chowdhury, M. Ying, L. Xu, M. Li, H.-J. Chung, H. Keum, M. McCormick, P. Liu, Y.-W. Zhang, F. G. Omenetto, Y. Huang, T. Coleman, J. A. Rogers, Epidermal electronics. *Science* **333**, 838–843 (2011).
37. M. Kaltenbrunner, T. Sekitani, J. Reeder, T. Yokota, K. Kuribara, T. Tokuhara, M. Drack, R. Schwödiauer, I. Graz, S. Bauer-Gogonea, S. Bauer, T. Someya, An ultra-lightweight design for imperceptible plastic electronics. *Nature* **499**, 458–463 (2013).
38. F. M. White, *Fluid Mechanics* (WCB McGraw-Hill Boston, ed. 4, 1999).
39. K. Sato, F. Sato, Individual variations in structure and function of human eccrine sweat gland. *Am. J. Physiol.* **245**, R203–R208 (1983).
40. T. C. Merkel, V. I. Bondar, K. Nagai, B. D. Freeman, I. Pinnau, Gas sorption, diffusion, and permeation in poly(dimethylsiloxane). *J. Polym. Sci. B* **38**, 415–434 (2000).
41. J.-M. Yang, G.-H. Hsue, Modified styrene-diene-styrene triblock copolymers for oxygen permeation. *Die Angewandte Makromolekulare Chemie* **231**, 1–14 (1995).
42. E. R. Nadel, R. W. Bullard, J. Stolwijk, Importance of skin temperature in the regulation of sweating. *J. Appl. Physiol.* **31**, 80–87 (1971).
43. M. Torii, M. Yamasaki, T. Sasaki, H. Nakayama, Fall in skin temperature of exercising man. *Br. J. Sports Med.* **26**, 29–32 (1992).
44. J. T. Korpelainen, K. A. Sotaniemi, V. V. Myllylä, Hyperhidrosis as a reflection of autonomic failure in patients with acute hemispherical brain infarction. An evaporimetric study. *Stroke* **23**, 1271–1275 (1992).
45. V. A. LeGrays, S. A. McColley, Z. Li, P. M. Farrell, The need for quality improvement in sweat testing infants after newborn screening for cystic fibrosis. *J. Pediatr.* **157**, 1035–1037 (2010).
46. D. A. Kidwell, J. C. Holland, S. Athanaselis, Testing for drugs of abuse in saliva and sweat. *J. Chromatogr. B Biomed. Sci. Appl.* **713**, 111–135 (1998).
47. J. Moyer, D. Wilson, I. Finkelshtein, B. Wong, R. Potts, Correlation between sweat glucose and blood glucose in subjects with diabetes. *Diabetes Technol. Ther.* **14**, 398–402 (2012).
48. Y. Y. Al-Tamer, E. A. Hadi, I. e. I. Al-Badrani, Sweat urea, uric acid and creatinine concentrations in uraemic patients. *Urol. Res.* **25**, 337–340 (1997).
49. C. J. Smith, G. Havenith, Body mapping of sweating patterns in athletes: A sex comparison. *Med. Sci. Sports Exerc.* **44**, 2350–2361 (2012).
50. N. A. Taylor, C. A. Machado-Moreira, Regional variations in transepidermal water loss, eccrine sweat gland density, sweat secretion rates and electrolyte composition in resting and exercising humans. *Extrem. Physiol. Med.* **2**, 4 (2013).

**Acknowledgments:** We thank the study participants for time and effort. We thank R. Randell, A. Reimel, and B. Sopena for conducting the data collection at the IRONMAN Triathlon World Championship and L. B. Baker for providing comments on the manuscript. **Funding:** This work was supported by the Center for Bio-Integrated Electronics of the Simpson Querrey Institute for BioNanotechnology. Funding for data collection at the IRONMAN Triathlon World Championship was provided by the Gatorade Sports Science Institute. **Author contributions:** J.T.R., J.C., and J.A.R. led the development of the concepts, designed the experiments, interpreted results, and wrote the paper. J.T.R. led the experimental work with support from J.C., P.G., J.H. M.L., T.R., A.J.B., and S.K. Y.X., R.A., W.X., and Y.H. performed the mechanical modeling and simulations. S.X., K.B., M.P., and R.G. contributed to the organization and design of the human trials and provided in-depth discussion. **Competing interests:** K.B. and M.P. are employed by the Gatorade Sports Science Institute, a division of PepsiCo Inc. The views expressed in this work are those of

the authors and do not necessarily reflect the position or policy of PepsiCo Inc. J.A.R., J.T.R., and J.C. are inventors on a Patent Cooperation Treaty (PCT) patent application submitted by the board of trustees of Northwestern University (PCT/US2018/35691; filed 1 June 2018). J.A.R. and R.G. are cofounders of Epicore Biosystems Inc., which pursues commercialization of epifluidic devices. J.A.R. currently serves as an associate editor on the editorial board of *Science Advances*. All other authors declare that they have no competing interests. **Data and materials availability:** All data needed to evaluate the conclusions in the paper are present in the paper and/or the Supplementary Materials. Additional data related to this paper may be requested from the authors.

Submitted 1 July 2018  
Accepted 10 December 2018  
Published 25 January 2019  
10.1126/sciadv.aau6356

**Citation:** J. T. Reeder, J. Choi, Y. Xue, P. Gutruf, J. Hanson, M. Liu, T. Ray, A. J. Bandodkar, R. Avila, W. Xia, S. Krishnan, S. Xu, K. Barnes, M. Pahnke, R. Ghaffari, Y. Huang, J. A. Rogers, Waterproof, electronics-enabled, epidermal microfluidic devices for sweat collection, biomarker analysis, and thermography in aquatic settings. *Sci. Adv.* **5**, eaau6356 (2019).

## Waterproof, electronics-enabled, epidermal microfluidic devices for sweat collection, biomarker analysis, and thermography in aquatic settings

Jonathan T. Reeder, Jungil Choi, Yeguang Xue, Philipp Gutruf, Justin Hanson, Mark Liu, Tyler Ray, Amay J. Bandodkar, Raudel Avila, Wei Xia, Siddharth Krishnan, Shuai Xu, Kelly Barnes, Matthew Pahnke, Roozbeh Ghaffari, Yonggang Huang and John A. Rogers

*Sci Adv* **5** (1), eaau6356.  
DOI: 10.1126/sciadv.aau6356

### ARTICLE TOOLS

<http://advances.sciencemag.org/content/5/1/eaau6356>

### SUPPLEMENTARY MATERIALS

<http://advances.sciencemag.org/content/suppl/2019/01/18/5.1.eaau6356.DC1>

### REFERENCES

This article cites 49 articles, 9 of which you can access for free  
<http://advances.sciencemag.org/content/5/1/eaau6356#BIBL>

### PERMISSIONS

<http://www.sciencemag.org/help/reprints-and-permissions>

Use of this article is subject to the [Terms of Service](#)

---

*Science Advances* (ISSN 2375-2548) is published by the American Association for the Advancement of Science, 1200 New York Avenue NW, Washington, DC 20005. 2017 © The Authors, some rights reserved; exclusive licensee American Association for the Advancement of Science. No claim to original U.S. Government Works. The title *Science Advances* is a registered trademark of AAAS.



## Supplementary Materials for

### **Waterproof, electronics-enabled, epidermal microfluidic devices for sweat collection, biomarker analysis, and thermography in aquatic settings**

Jonathan T. Reeder, Jungil Choi, Yeguang Xue, Philipp Gutruf, Justin Hanson, Mark Liu, Tyler Ray, Amay J. Bandodkar, Raudel Avila, Wei Xia, Siddharth Krishnan, Shuai Xu, Kelly Barnes, Matthew Pahnke, Roozbeh Ghaffari, Yonggang Huang, John A. Rogers\*

\*Corresponding author. Email: [jrogers@northwestern.edu](mailto:jrogers@northwestern.edu)

Published 25 January 2019, *Sci. Adv.* **5**, eaau6356 (2019)  
DOI: 10.1126/sciadv.aau6356

#### **This PDF file includes:**

- Fig. S1. NFC coil components.
- Fig. S2. Environmental backfilling due to hydrostatic pressure and impact.
- Fig. S3. Aging of SIS rendered hydrophilic by UVO treatment.
- Fig. S4. Setup for measuring flow rates through SIS-based microfluidic systems.
- Fig. S5. Filling rates at physiological pressures.
- Fig. S6. Experimental setup for comparison of evaporation rate of sweat after collection.
- Fig. S7. Mechanical effect of tapered edge and SIS thickness.
- Fig. S8. Effect of deformation on apparent sweat volume.
- Fig. S9. Impact of adhesive geometry on sweat collection.
- Fig. S10. Details for the trial with IRONMAN triathletes.
- Fig. S11. Influence of epidermal sweat device on heat and sweat generation during biking.

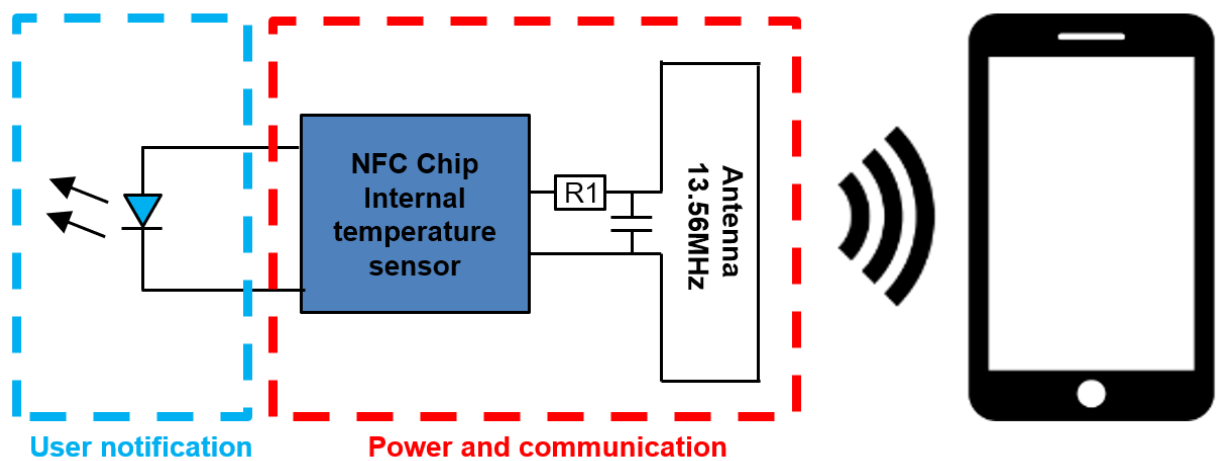


**Fig. S1. NFC coil components.** The circuit diagram for skin temperature readout and user notification.

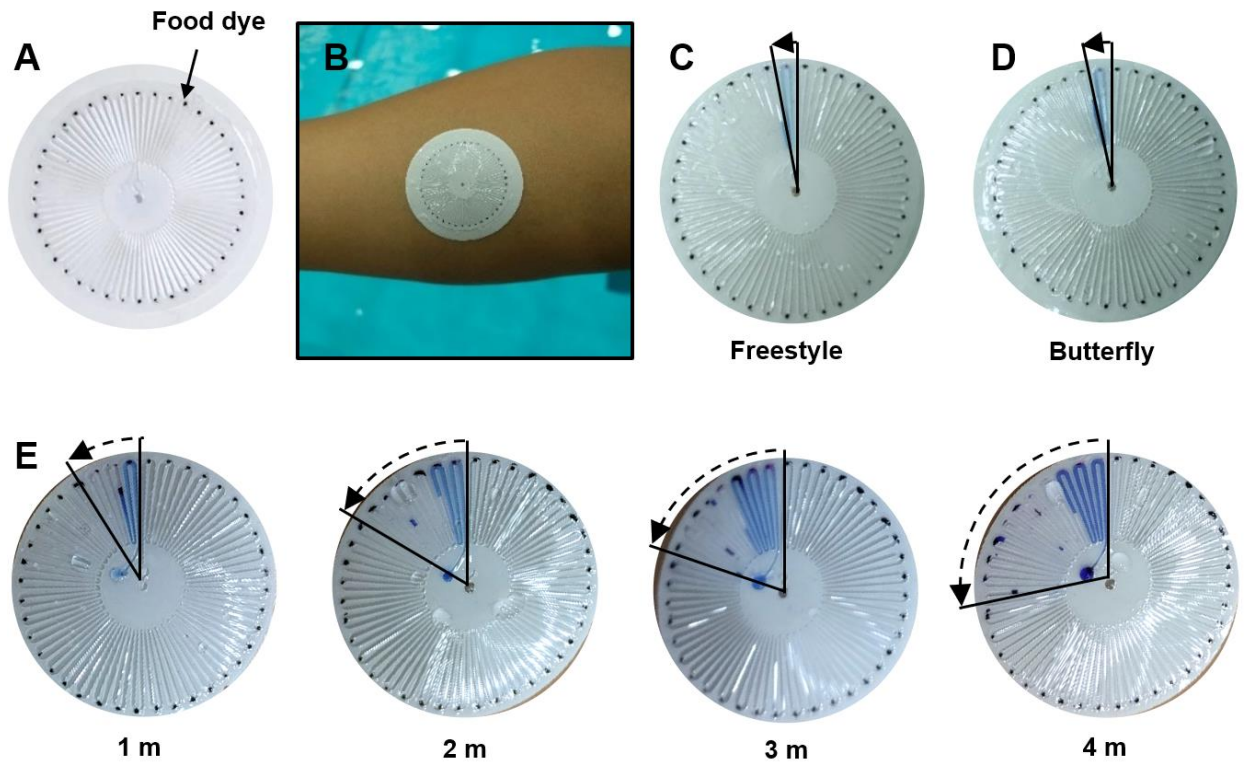


**Fig. S2. Environmental backfilling due to hydrostatic pressure and impact.** **A)** Pictures of a device used for testing effects of backfilling due to water in the environment. Food dye deposited at the top of each turn in the microfluidic channel facilitates visual readout of the extent to which environmental water progressed into the channel structure from the outlet. **B)** The device after attaching to the forearm. **C)** Backfilling of a device after swimming 100 m of freestyle. **D)** Backfilling of a device after swimming 100 m of butterfly. **E)** Backfilling of a device after submerging at various depths. Images were taken after remaining at depth for 10-15 s and then returning to the surface. Incomplete ejection of backfilled fluid after surfacing is due to capillary forces. (Photo credit: J. Reeder, Northwestern University)



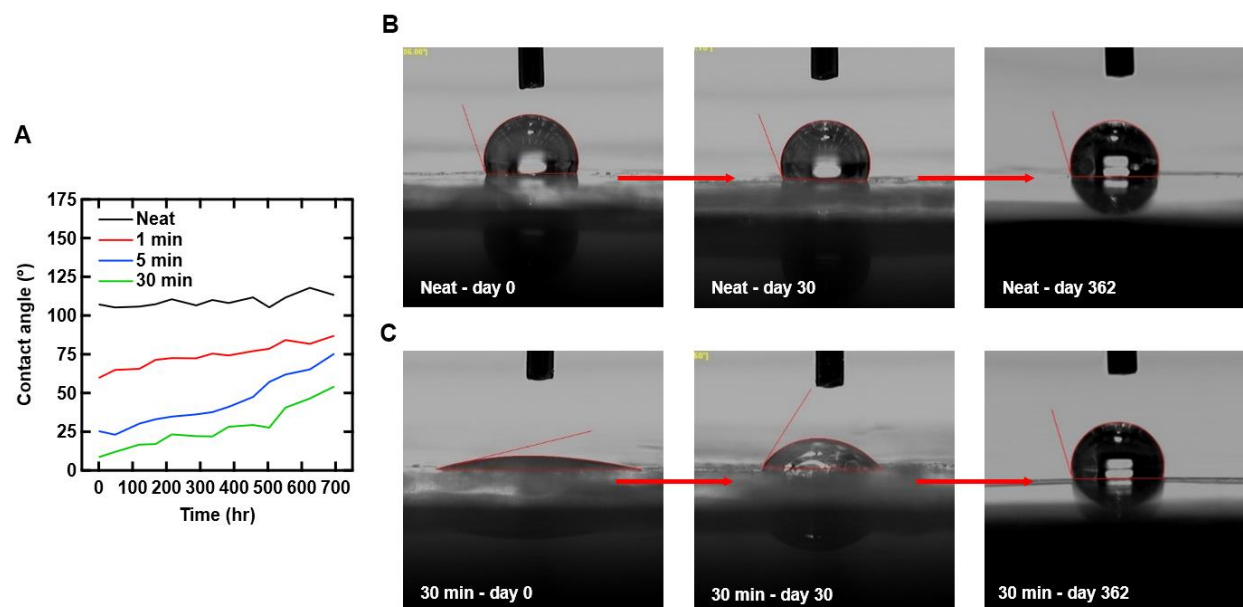


**Fig. S3. Aging of SIS rendered hydrophilic by UVO treatment.** **A)** Time evolution of contact angle of SIS in ambient air after treating with UV ozone for 1, 5, and 30 min. **B)** The aging of the contact angle of water on neat SIS. **C)** The aging of the contact angle of water on SIS treated with 30 min of UV ozone. (Photo credit: M. Liu, Northwestern University)

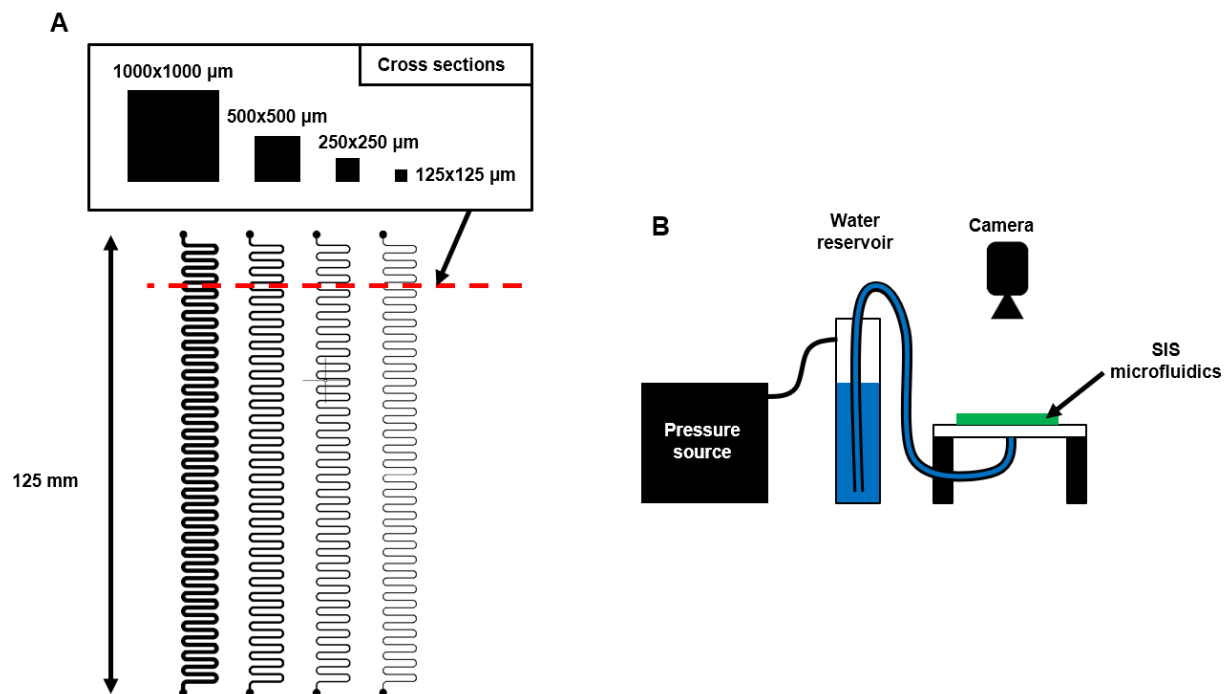


**Fig. S4. Setup for measuring flow rates through SIS-based microfluidic systems. A) Channel geometry for microfluidic flow rate test samples. B) Experimental setup for measuring fluid flow rate.**

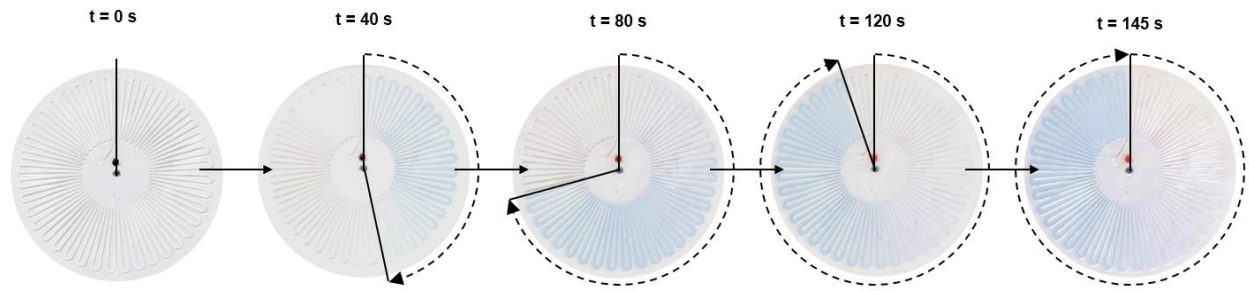


**Fig. S5. Filling rates at physiological pressures.** The progression of fluid through an epifluidic device due to an applied pressure of 2 kPa at the inlet. The 60  $\mu\text{l}$  device fills in 145 s, corresponding to an average rate of 25  $\mu\text{l}/\text{min}$ .



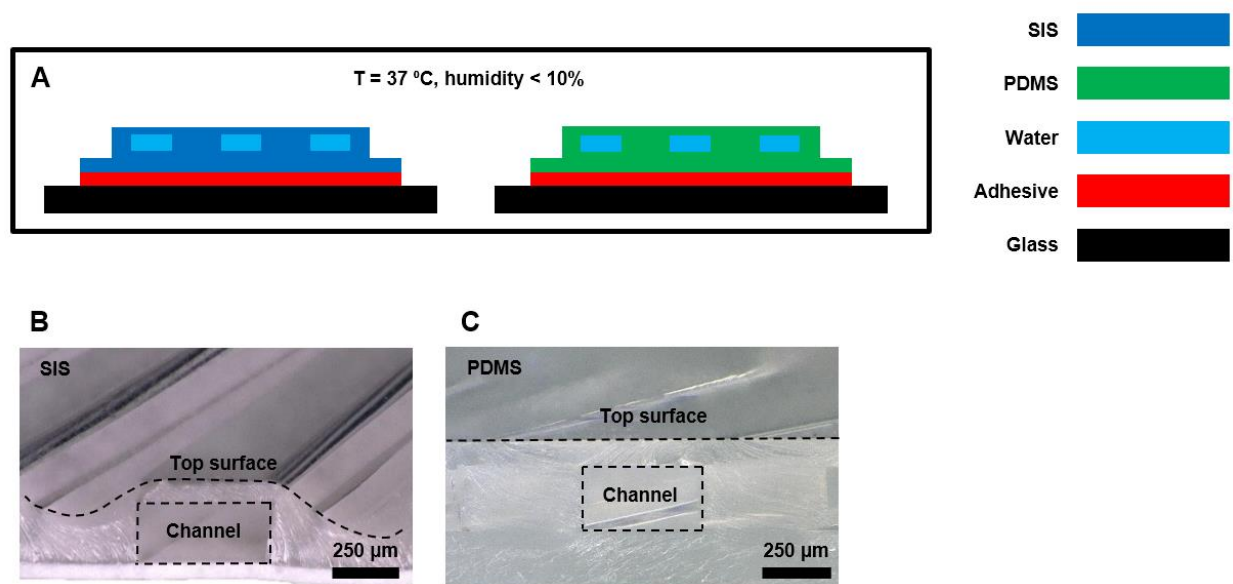


**Fig. S6. Experimental setup for comparison of evaporation rate of sweat after collection.** A) Experimental setup for measuring evaporative water loss from epifluidic devices. B) Cross-sectional micrograph of an SIS device. C) Cross-sectional micrograph of a PDMS device.

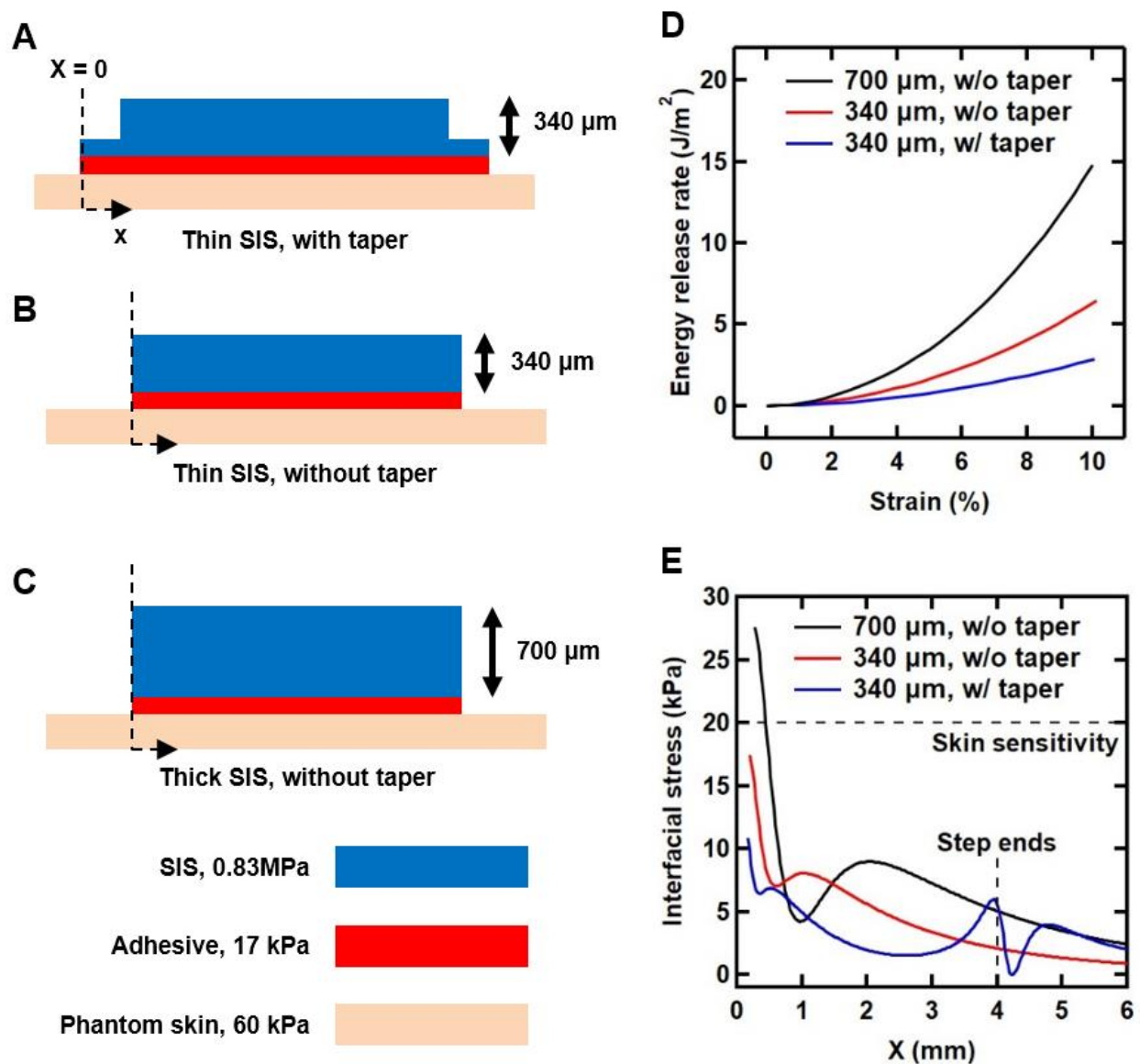


**Fig. S7. Mechanical effect of tapered edge and SIS thickness.** **A)** Cross-sectional illustration of a SIS device with thickness of 340  $\mu\text{m}$  and a tapered edge. **B)** Cross-sectional illustration of a similar device but without the tapered edge. **C)** Cross-sectional illustration of a SIS device with thickness of 700  $\mu\text{m}$ , without a tapered edge. **D)** Modeling results for the energy release rate for these three types of devices for applied strains of up to 10%. **E)** Modeling results for interfacial stress as a function of distance from the center of the device when stretched by 10%.

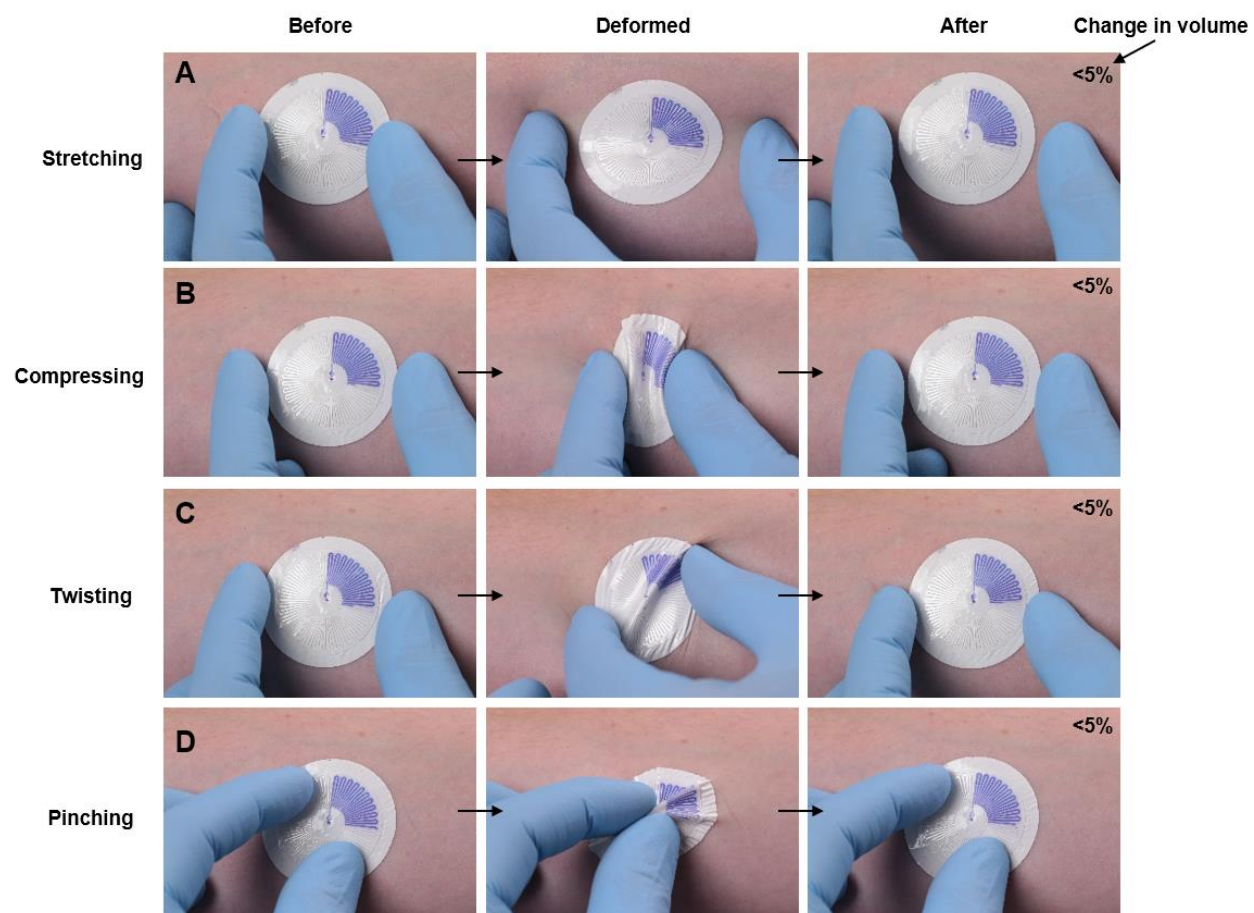


**Fig. S8. Effect of deformation on apparent sweat volume. A) Stretching. B) Compressing. C) Twisting. D) Pinching.** (Photo credit: J. Choi, Northwestern University)

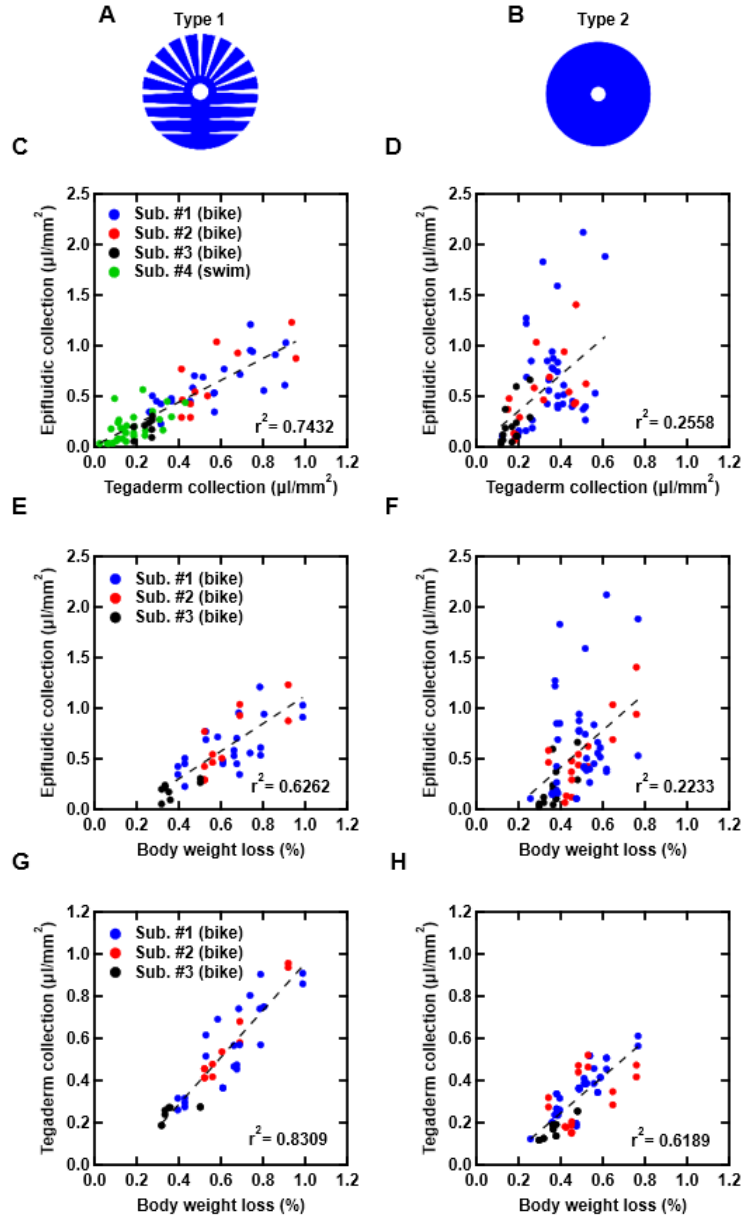


**Fig. S9. Impact of adhesive geometry on sweat collection.** A) Type 1 adhesive geometry with  $r = 3$  mm collection area and radial vents to decrease compensatory sweating. The non-symmetrical feature at the bottom enables easy removal of the adhesive backing. B) Type 2 adhesive geometry with  $r = 3$  mm collection area. C) and D) show the volume of sweat collected with devices with Type 1 and Type 2 adhesives, respectively, as compared to sweat volume collected via an absorbent pad. E) and F) show the volume collected using devices with Type 1 and Type 2 adhesive, as compared to % body weight loss. G) and H) Show a comparison of sweat volume collected via absorbent pads to % body weight loss for the trials using the Type 1 and Type 2 adhesive.



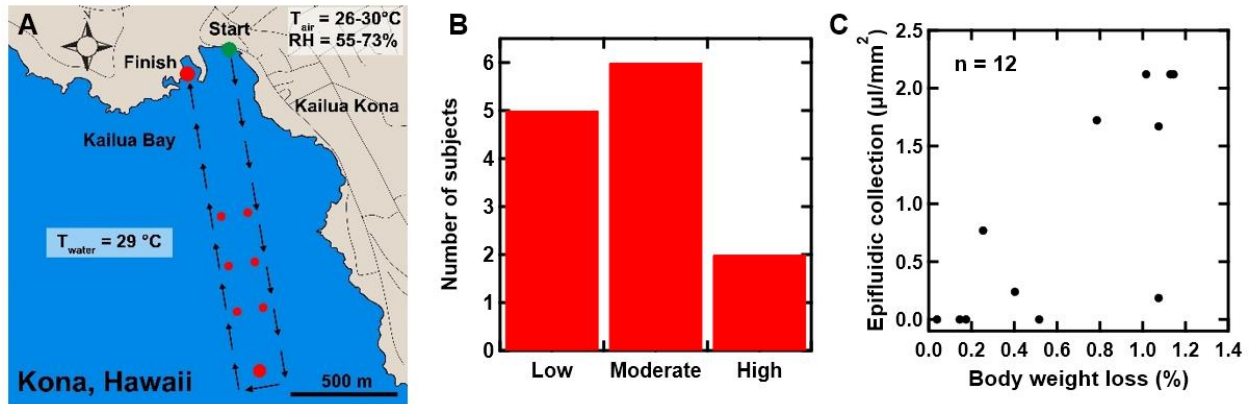


**Fig. S10. Details for the trial with IRONMAN triathletes.** **A)** Map of the route for a swimming trial in Kona, HI. **B)** Self-reported swim intensity for the 12 subjects. The average swim time was 45 min. **C)** Comparison of sweat volume collected during swimming via epifluidic device with measurements of % body weight loss. Inadvertent water gains and losses via spitting, drinking water, etc prevents good correlation between local sweat volume collection and body weight changes.

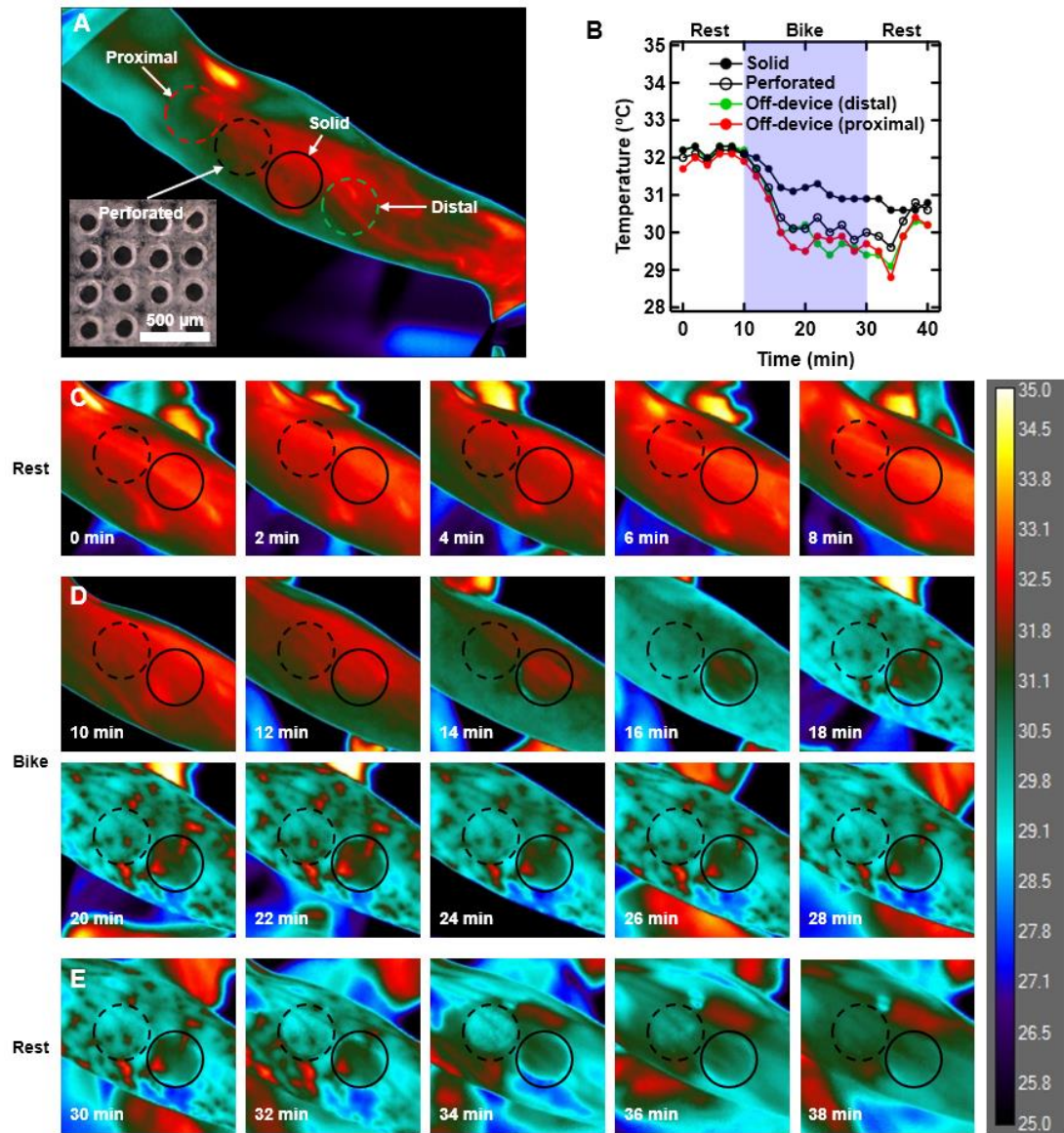


**Fig. S11. Influence of epidermal sweat device on heat and sweat generation during biking.** **A)** Experimental setup showing the location of the devices on the forearm, as well as proximal and distal temperature sampling areas. The perforated device includes an array of laser-drilled 125  $\mu\text{m}$  diameter holes with 250  $\mu\text{m}$  pitch (inset). **B)** Temperature response of the forearm during biking. The temperature was averaged over the sampling area. **C)** The results show negligible localization of heat under either device while resting. **D)** Exercise induces increases in the temperature of the skin under the solid device, but not the perforated device. Sweating begins after ~6 min of exercise and decreases the temperature of the skin. **E)** Hot spots dissipate after ~10 min of resting.